



Late-orogenic Evolution of the Southern European Variscan Belt Constrained by Fabric Analysis and Dating of the Camarat Granitic Complex and Coeval Felsic Dykes (Maures–Tanneron Massif, SE France)

Olivier Bolle, Michel Corsini, Hervé Diot, Oscar Laurent, Raphaël Melis

► To cite this version:

Olivier Bolle, Michel Corsini, Hervé Diot, Oscar Laurent, Raphaël Melis. Late-orogenic Evolution of the Southern European Variscan Belt Constrained by Fabric Analysis and Dating of the Camarat Granitic Complex and Coeval Felsic Dykes (Maures–Tanneron Massif, SE France). *Tectonics*, 2023, 42 (4), pp.e2022TC007310. 10.1029/2022TC007310 . hal-04060234

HAL Id: hal-04060234

<https://hal.science/hal-04060234>

Submitted on 7 Dec 2023

HAL is a multi-disciplinary open access archive for the deposit and dissemination of scientific research documents, whether they are published or not. The documents may come from teaching and research institutions in France or abroad, or from public or private research centers.

L'archive ouverte pluridisciplinaire **HAL**, est destinée au dépôt et à la diffusion de documents scientifiques de niveau recherche, publiés ou non, émanant des établissements d'enseignement et de recherche français ou étrangers, des laboratoires publics ou privés.

Copyright

Tectonics®

RESEARCH ARTICLE

10.1029/2022TC007310

Key Points:

- The Camarat Granitic Complex and late felsic dykes were emplaced in the Internal Zone of the Maures–Tanneron Massif at ~305–298 Ma
- Emplacement of the Camarat Granitic Complex and coeval felsic dykes was concomitant with the late stages of a transpressive tectonic phase
- An orogen-parallel crustal flow was prevailing from late Carboniferous transpression to early Permian extension in the SE Variscides

Supporting Information:

Supporting Information may be found in the online version of this article.

Correspondence to:

O. Bolle,
olivier.bolle@uliege.be

Citation:

Bolle, O., Corsini, M., Diot, H., Laurent, O., & Melis, R. (2023). Late-orogenic evolution of the Southern European Variscan Belt constrained by fabric analysis and dating of the Camarat Granitic Complex and coeval felsic dykes (Maures–Tanneron Massif, SE France). *Tectonics*, 42, e2022TC007310. <https://doi.org/10.1029/2022TC007310>

Received 14 MAR 2023

Accepted 10 MAR 2023

Author Contributions:

Conceptualization: Olivier Bolle, Michel Corsini

Formal analysis: Olivier Bolle, Michel Corsini, Hervé Diot, Oscar Laurent

Investigation: Olivier Bolle, Michel Corsini, Hervé Diot, Oscar Laurent, Raphaël Melis

Project Administration: Olivier Bolle, Michel Corsini

Resources: Olivier Bolle, Michel Corsini, Hervé Diot, Raphaël Melis

Supervision: Olivier Bolle, Michel Corsini

Visualization: Olivier Bolle, Michel Corsini, Oscar Laurent

Writing – original draft: Olivier Bolle, Michel Corsini, Oscar Laurent

Late-Orogenic Evolution of the Southern European Variscan Belt Constrained by Fabric Analysis and Dating of the Camarat Granitic Complex and Coeval Felsic Dykes (Maures–Tanneron Massif, SE France)

Olivier Bolle^{1,2} , Michel Corsini³, Hervé Diot^{4,5}, Oscar Laurent^{6,7} , and Raphaël Melis^{3,8}

¹Département de Géologie, Université de Liège, Liège, Belgium, ²FNRS, Brussels, Belgium, ³Université Côte d'Azur, IRD, CNRS, Observatoire de la Côte d'Azur, Valbonne, France, ⁴UMR-CNRS 6112, Laboratoire de Planétologie et Géosciences, Université de Nantes, Nantes, France, ⁵LASIE, Université de La Rochelle, La Rochelle, France, ⁶ETH Zürich, Department of Earth Sciences, Institute for Geochemistry and Petrology, Zürich, Switzerland, ⁷Now at Géosciences Environnement Toulouse, UMR-CNRS 5563, Toulouse, France, ⁸Now at LGL-TPE, UMR-CNRS 5276, Université Claude Bernard, Lyon 1, Villeurbanne, France

Abstract The Camarat Granitic Complex (CGC), emplaced in the migmatitic Internal Zone of the Maures–Tanneron Massif (MTM), SE Variscides, consists of the Gigaro granodiorite and the composite Camarat granite. U-Pb dating of the latter gives crystallization ages of 304.5 ± 3.3 Ma (zircon date) and 303.5 ± 4.0 Ma (monazite date). Two representatives of late felsic dykes cutting across the MTM Internal Zone have $^{39}\text{Ar}/^{40}\text{Ar}$ muscovite ages of 302.43 ± 2.62 Ma and 298.11 ± 2.38 Ma. Magmatic lineations revealed by anisotropy of magnetic susceptibility (AMS) measurements and image analysis, aplite dykes, dyke-like bodies of cordierite microgranite and joints in the Camarat granite, as well as the late dykes all have orientations consistent with subhorizontal, NNE-SSW-trending lineations in the migmatitic country rocks representing the stretching direction of a late-Variscan transpression phase (D_3). The CGC and the late dykes are therefore witness to a thermal event that affected the MTM between ~305 and ~298 Ma (late Pennsylvanian–earliest Permian times), at the end of D_3 which initiated at ~325 Ma. Grabens related to post-Variscan, Permian rifting (D_4 phase), which cut across the MTM are WNW-ESE-trending, indicating a NNE-SSW direction of extension, parallel to the previous (D_3) lateral horizontal flow. The present results and a comparison with AMS data published for the Corsica–Sardinia Batholith reveal that evolution in the SE Variscides from Devonian–early Carboniferous contraction to Permian extension, through late Carboniferous transpression is characterized by the persistence of a ca. N-S stretching direction, supporting a strong horizontal, orogen-parallel crustal flow.

1. Introduction

The Devonian–Carboniferous European Variscan Belt or Variscides formed as a consequence of the convergence between Laurussia to the north and Gondwana to the south (present-day orientation), closure of intervening oceanic basins and accretion of various terranes (e.g., Franke et al., 2017; Martínez Catalán et al., 2021; Matte, 2001; Vanderhaeghe et al., 2020). The geodynamic evolution of the Variscides and its geological implications can be tentatively summarized as follows (Domeier & Torsvik, 2014; Edel et al., 2018; Franke et al., 2017; Matte, 2001; Ziegler & Stampfli, 2001): (a) Devonian–early Carboniferous subduction and collisional events, leading to nappe stacking and subsequent crustal thickening; (b) late Carboniferous to early Permian dextral wrenching, following oblique convergence, between Gondwana and Laurussia, with reactivation or formation of crustal-scale strike-slip faults/shear zones, emplacement of large volumes of granitoids and creation of narrow intracontinental basins accompanied by bimodal magmatism; and (c) around the middle Permian, generalized extension at the onset of opening of the Neotethys Ocean, resulting in the development of gradually expanding sedimentary basins, which marks the beginning of the Alpine sedimentary cycle. In this evolution scheme, the late Carboniferous–early Permian tectonics is considered to be extensional/transensional for most of the Variscides, a feature classically attributed to the gravitational collapse of the Variscan Belt (e.g., Edel et al., 2018; Faure et al., 2009; Vanderhaeghe et al., 2020). However, in the SE branch of the Variscides, that is, Maures–Tanneron Massif (MTM), Corso–Sardinian Block and Alpine External Crystalline Massifs, affected to the east by a crustal-scale high-strain zone resulting from transpressional movements along the Gondwana margin (Bellot, Bronner, & Laverne, 2002; Corsini & Rolland, 2009; Guillot & Ménot, 2009; Matte, 2001; Simonetti

Writing – review & editing: Olivier Bolle, Michel Corsini, Hervé Diot, Oscar Laurent

et al., 2020), it has been proposed that extensional movements during the late Carboniferous may equally have been produced by exhumation of deep-crustal rocks along transcurrent shear-zones (Corsini & Rolland, 2009; Rolland et al., 2009). Also, the emplacement of numerous Variscan granitoids have been channeled by strike-slip structures (Casini, Cuccuru, Puccini, et al., 2015; Rolin et al., 2009) and strike-slip faults are known to have controlled location of many late Paleozoic intracontinental basins (Arthaud & Matte, 1977; Cassinis et al., 2012). The late Carboniferous–early Permian is thus a pivotal period in the late- to post-orogenic evolution of the Variscides, which corresponds to the transition from a convergence context during Devonian–early Carboniferous to a diverging setting from middle Permian and later, with large-scale strike-slip structures that promoted magmatism and extensional tectonics.

The MTM, as most of the Corso–Sardinian Block, but contrary to the Alpine External Crystalline Massifs, has escaped reworking during the Alpine orogeny and is therefore a key area for the study of the SE Variscides. The eastern segment of the MTM, strongly affected by the transpressive tectonics (Corsini & Rolland, 2009; Schneider et al., 2014; Simonetti et al., 2020), is intruded by syn- to late-orogenic granitoids (Crevola et al., 1991; Duchesne et al., 2013; Onézime et al., 1999) and the whole massif has been dissected by small late Carboniferous intramontane coal-bearing basins and larger Permian grabens (Durand, 2008; Toutin-Morin et al., 1993) which are representatives of the European late Paleozoic intracontinental basins.

Here, we present a fabric study of the Camarat granite (Amenzou & Pupin, 1986), using the anisotropy of magnetic susceptibility (AMS) technique, supported by thermomagnetic experiments and image analysis (IA), and combined with geochronology (U–Pb zircon and monazite dating of the granite, and Ar/Ar dating of potentially contemporaneous late felsic dykes). The Camarat granite is a small composite igneous body which was emplaced in the MTM in late Carboniferous times, during the transition between late-Variscan transpression and Permian extension according to Gerbault et al. (2018). We will use this granite as a structural marker to better constrain the regional tectonics of this pivotal period. A comparison will also be made with AMS data published for granitoids of similar ages from the Corso–Sardinian Variscan basement.

2. Geological Setting of the Maures–Tanneron Massif

2.1. General Framework

The MTM is composed of the Maures Massif to the south and the Tanneron Massif to the north, separated by a ca. E–W Permian rift (Figure 1b). It can be subdivided into two ca. N–S-trending metamorphic domains (Schneider et al., 2014): a very-low- to medium-grade External Zone to the west and a high-grade, migmatitic Internal Zone to the east. The External Zone consists of mostly metasedimentary series and a large metagranodioritic unit (the Bormes orthogneiss), with a prograde Barrovian metamorphism increasing eastwards from the chlorite zone to the kyanite zone, whereas the Internal Zone is predominantly made of migmatitic para- and orthogneisses that contain lenses of metabasic rocks with relics of HP–LT (eclogite-facies) metamorphism and serpentinized mantle-derived peridotites (review in Bellot, 2005).

The two domains are separated by the regional-scale La Garde-Freinet–Cavalaire “Fault” (Figure 1b), which is a west-dipping shear zone (Bellot, Bronner, Marchand, et al., 2002), considered as the major suture of the MTM (Gerbault et al., 2018; Schneider et al., 2014) and reactivated as a transpressive shear zone (Simonetti et al., 2020). The External Zone is subdivided into a very-low to low-grade unit to the west and a medium-grade unit to the east by another east-verging major shear zone, the Collobrières “Fault,” whereas two major, ca. N–S and steeply dipping late strike-slip shear zones, the Grimaud–Joyeuse and La Moure “faults,” crosscut the whole Internal Zone (Figure 1b; Vauchez & Bufalo, 1985; Rolland et al., 2009; Schneider et al., 2014). At the regional scale, the MTM is characterized by upright folds with ca. N–S-trending axes, which deform the main metamorphic foliation and are mostly known in the Internal Zone (Bellot, 2005; Crevola et al., 1991; Rolland et al., 2009).

Two suites of Variscan granitoids crops out in the Internal Zone (Figure 1b; Crevola et al., 1991; Duchesne et al., 2013): a minor, variably deformed, dominantly tonalitic syn-orogenic (Visean) suite and a late-orogenic (late Carboniferous) suite with a peraluminous character. The largest late-Variscan pluton is by far the Plan-de-la-Tour granite and its prolongation in the Tanneron Massif, the Rouet granite, which are elongated along the Grimaud–Joyeuse Fault (Figure 1b). Basic (mostly dolerite) and felsic (mostly granitic), cm- to 10-m-scale dykes, generally ca. E–W-trending, cut across the migmatitic gneisses and the granitoids throughout the Internal Zone (e.g., Bordet et al., 1967; Toutin-Morin et al., 1994).

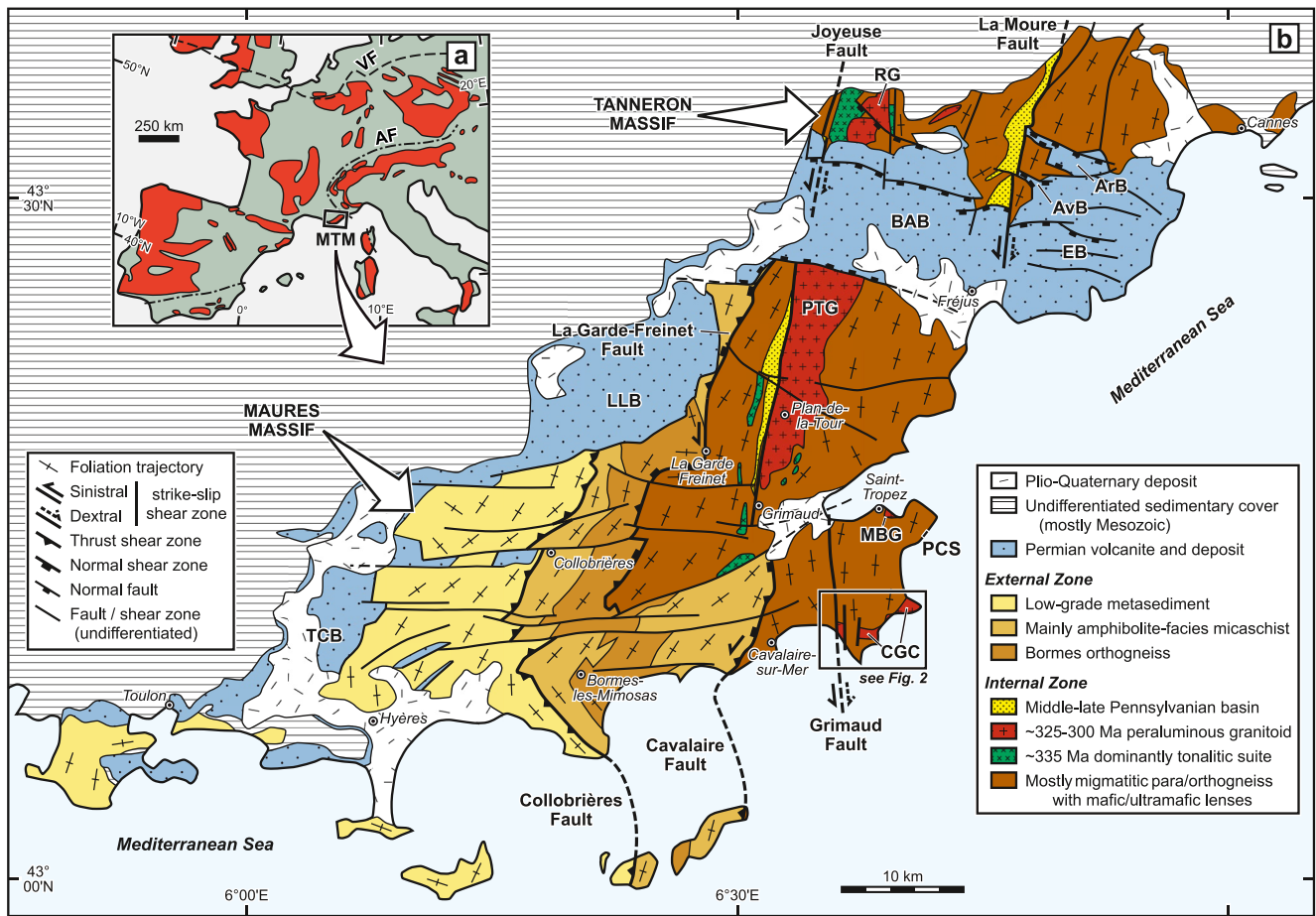


Figure 1. Geology of the Maures–Tanneron Massif (MTM). (a) Distribution map of Variscan units in Western Europe (simplified from Franke (1989) and Franke et al. (2017)), with location of the MTM; AF, Alpine deformation front; VF, Variscan deformation front (northern Variscan external front; see Figure 14b). (b) Simplified geological map of the MTM (modified from Rouire, Bodelle, et al. (1979), Rouire, L'Homer, et al. (1979); with additional structural and lithological data from Crevola et al. (1991), Toutin-Morin et al. (1993), Bellot (2005), Corsini and Rolland (2009), and Schneider et al. (2014), and references therein; ages of granitoids are U-(Th)-Pb dates from references in the text and from the present study); ca. N-S major “faults” are actually shear zones with a protracted and polyphase history ending with brittle-ductile to brittle movements; undifferentiated faults with an important sinistral strike-slip component that cut across the Maures Massif are inherited Permian faults, probably reactivated during Pyrenean orogeny; ArB and AvB, Argentièrre and Avellan basins; BAB, Bas-Argens basin; CGC, Camarat Granitic Complex; EB, Estérel basin; LLB, Le Luc basin; MBG, Moulin Blanc granite; PCS, Pinet–Capon section; PTG, Plan-de-la-Tour granite; RG, Rouet granite; TCB, Toulon–Cuers basin.

Middle to Late Pennsylvanian, intramontane coal-bearing basins are located along the Grimaud–Joyeuse and La Moure faults (Figure 1b; Toutin-Morin et al., 1993; Bellot, 2005). The MTM is also cut and bordered by ca. E-W Permian grabens filled with continental sediments and volcanic rocks (Figure 1b; e.g., Toutin-Morin et al., 1993). The volcanism is bimodal, however dominated by the felsic (rhyolitic) pole and has an alkaline geochemical signature, with the notable exception of the oldest (earliest Permian), minor mafic rocks that are calc-alkaline (references in Durand, 2008). No important strike-slip movement has been detected along normal faults, at least for the well-exposed grabens separating the Maures and Tanneron massifs (Toutin-Morin & Bonijoly, 1992). On the contrary, ca. E-W inherited Permian normal faults that cut across the Maures Massif display a locally large, up to several kilometers, sinistral strike-slip displacement (Figure 1b), probably associated with the Pyrenean orogeny (Toutin-Morin et al., 1994).

2.2. Variscan Tectono-Metamorphic Events

The Variscan tectono-metamorphic evolution of the MTM is polyphasic. We will retain here the most recent evolution scheme of Schneider et al. (2014) and Gerbault et al. (2018). A late Ordovician–Silurian to early Devonian oceanic subduction is testified, among others, by the relics of eclogite-facies metamorphism (M_0) found in

the Internal Zone. The P - T conditions of M_0 have not been estimated yet. This subduction was followed, during the Devonian–Mississippian, by continental subduction and collision, leading to NW-directed nappe tectonics (D_1), then backthrusting of the nappes toward the SE (D_2). The D_1 and D_2 phases are mostly preserved in the External Zone, where the main (flat-lying) foliation, as well as the Collobrières and La Garde-Freinet–Cavalaire faults are inherited from the nappe tectonics. Peak conditions of MP-MT to HT, Barrovian-type metamorphism (M_1 - M_2) increase from west to east, from 4 to 6 kbar and 430 to 650°C (Bellot et al., 2003; Buscail, 2000). During the Pennsylvanian, the Internal Zone was affected by a highly partitioned transpression (D_3 phase), with a ca. E-W shortening producing the regional-scale, N-S-trending upright folds with a subvertical axial-plane S_3 foliation and a ca. N-S strike-slip shearing being localized along discontinuities such as the Grimaud–Joyeuse and La Moure faults (Corsini & Rolland, 2009). The D_3 transpression was associated with exhumation of the metamorphic units, LP-HT metamorphism (M_3) and generalized partial melting, as well as formation of the late Carboniferous intra-montane coal-bearing basins controlled by the Grimaud–Joyeuse and La Moure strike-slip faults (Bellot, 2005; Rolland et al., 2009). In the External Zone, D_3 corresponds to a collapse phase controlled by the Collobrières and La Garde-Freinet–Cavalaire faults, associated with a LP-LT M_3 retrograde metamorphic phase. P - T conditions of M_3 were estimated at 2–4 kbar and 500–350°C in metabasites of the Internal zone (Bellot et al., 2003).

The post-Variscan, Permian tectonic evolution of the MTM is largely dominated by a localized, ca. N-S extension (D_4 phase of Gerbault et al., 2018), creating the ca. E-W grabens. Following Toutin-Morin and Bonijoly (1992), the Permian extensional tectonics became prominent, with foundering of the basins, around the early–middle Permian boundary. Generalized extension, hence the Alpine sedimentary cycle began at the Permo-Triassic transition in the MTM area (e.g., Durand, 2008).

2.3. Magmatic Evolution: Summary of Main Geochronological Constraints

Robust evidence of pre- to early-Variscan magmatism, through combined U-(Th)-Pb dating and geochemical data are scarce in the MTM metamorphic rocks: an age of ~590 Ma in the high-K calc-alkaline granodioritic Bormes orthogneiss constrains an Ediacarian continental arc magmatism (Tabaud et al., 2022), a late Ediacarian–Cambrian bimodal magmatic event during continental rifting is supported by an age of 548 ± 17 –7 Ma obtained on an alkaline leptyno-amphibolitic complex of the Maures External Zone (Innocent et al., 2003) and an age of 456 ± 11 found in a calc-alkaline orthogneiss from the Tanneron Internal Zone is so far one the best evidence of an early-Variscan oceanic subduction-related magmatism (Oliot et al., 2015).

The dominantly tonalitic, syn-Variscan granitoids are dated at 338 ± 6 to 334 ± 3 Ma (zircon U-Pb ages; Moussavou, 1998) and the late-Variscan granitoid suite have emplacement ages between 329 ± 3 and 301 ± 2 Ma (zircon and monazite U-(Th)-Pb dates; Demoux et al., 2008; Duchesne et al., 2013; Oliot et al., 2015). These two granitoid suites are coeval, respectively, with the D_2 and D_3 phases (Gerbault et al., 2018; Schneider et al., 2014). It is worth noting that D_3 strike-slip shear zones such as the Grimaud–Joyeuse Fault had an important control on the emplacement of the granitoids, as exemplified by the Plan-de-la-Tour–Rouet granitic complex (Onézime et al., 1999). The basic dykes found in the MTM Internal Zone are traditionally attributed to Permian volcanism (e.g., Zheng et al., 1992). However, at least some of them, as well as many felsic dykes are representative of the late-Variscan magmatism, according to geochronological, petrological and/or structural data (Demoux et al., 2008; Duchesne et al., 2013).

In the Permian rift, emplacement of the largest ignimbritic rhyolite was dated at 272.5 ± 0.3 Ma ($^{40}\text{Ar}/^{39}\text{Ar}$ Ar weighted mean age; Zheng et al., 1992), which corresponds to the early–middle Permian boundary.

3. The Camarat Granitic Complex

3.1. Field Observations

The Camarat granite was formerly described as a single E-W-trending body made of muscovite-biotite granite, bounded and mylonitized to the west by the Grimaud Fault and cut by numerous faults of unspecified age (Bordet et al., 1967). However, according to Amenjou and Pupin (1986), this intrusion consists of several small bodies with distinct petrographical and geochemical characteristics. Our field work, supported by a petrographical analysis, confirms this interpretation and complements the observations of Amenjou and Pupin (1986). In particular, our observations allowed to clearly delineate the limits of the small bodies, to precisely characterize the rock facies and their distribution, and to decipher the structural pattern of the country rocks (Figure 2).

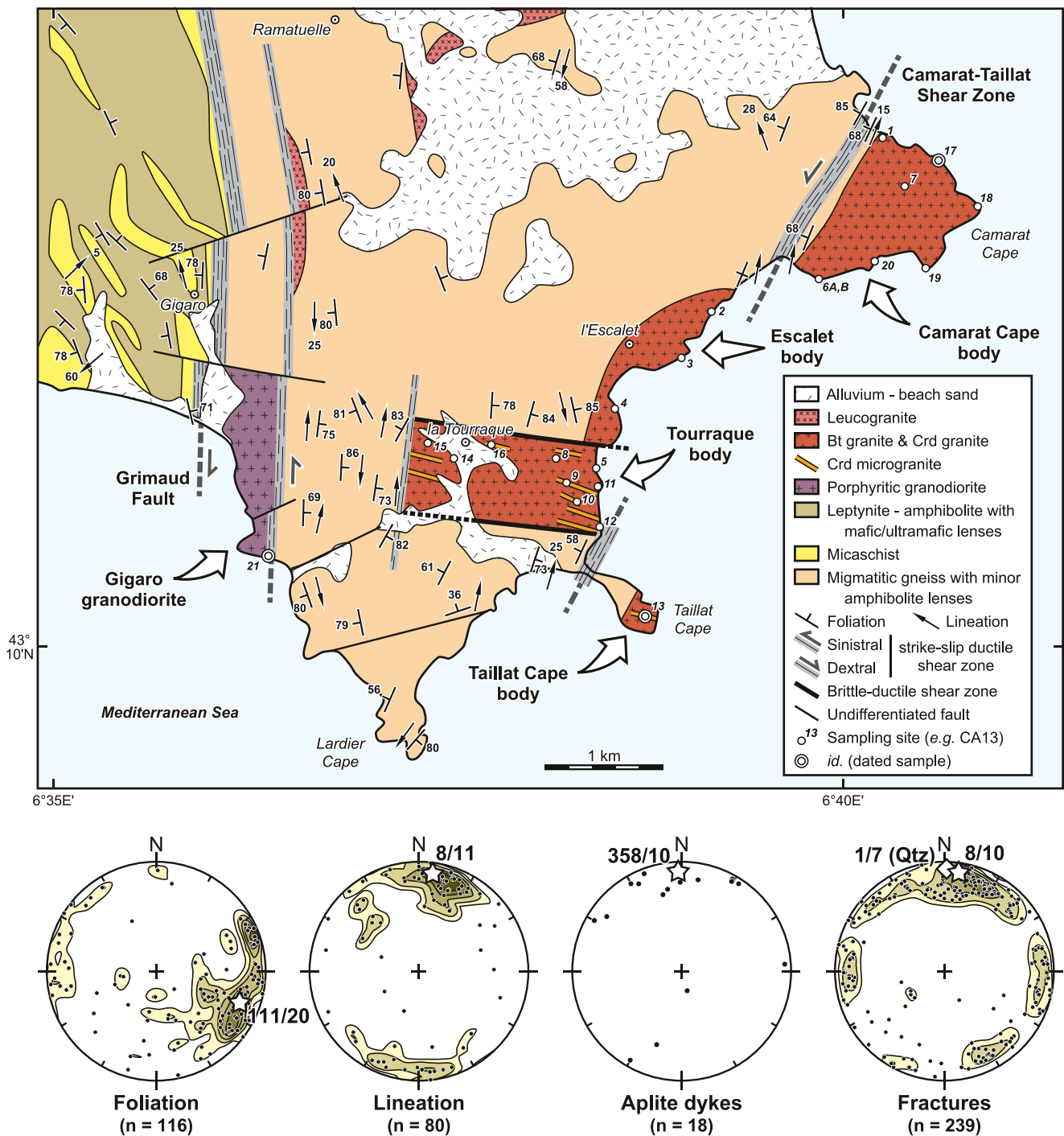


Figure 2. Geological and structural map of the Camarat Granitic Complex (Gigaro granodiorite and Camarat granite made of the Camarat Cape, Escalet, Tourraque and Taillat Cape bodies) and its country rocks, with selected foliation and lineation measurements (Bordet et al., 1967; Amenou & Pupin, 1986; modified according to observations of the authors). Undifferentiated transversal faults correspond to inherited Permian faults, probably reactivated during Pyrenean orogeny. Plots are lower hemisphere, equal-area projections showing poles of the gneissic foliation, mineral and stretching lineation from the gneisses, and poles of aplite dykes and fractures (mainly joints) cutting across the Camarat granite (contours at 1-2-3-4-5% for the foliation, and 1-2-4-6-8%) for the lineation and the joints; white star: weighted mean; white diamond: weighted mean of four elongation measurements of quartz—Qtz—grains within E-W fractures at the boundary between the Escalet and Tourraque bodies)).

The westernmost intrusion is the Gigaro granodiorite of Amenzou and Pupin (1986), a possible southward prolongation of the Plan-de-la-Tour–Rouet granitic complex according to these authors. The Gigaro granodiorite consists of a N-S-trending intrusion buried below the Mediterranean Sea to the SW (outcrop < 1 km²), dominantly made of a porphyritic biotite granodiorite containing megacrysts of alkali feldspars. Further east, the Camarat granite sensu Amenzou and Pupin (1986) is a fine- to coarse-grained, two-mica (\pm cordierite) granite. The Camarat granite forms three bodies along the coast, respectively in the Camarat Cape, l'Escalet and Taillat Cape areas, and also an E-W strip close to la Tourraque (Figure 3a). These four granitic bodies outcrop on a total surface of \sim 3 km². In the present study, we will focus on the fabric of the Camarat granite sensu Amenzou and Pupin (1986), hence on the Camarat Cape, Escalet, Tourraque and Taillat Cape bodies which, together with the Gigaro granodiorite, will be referred collectively as to the Camarat Granitic Complex (CGC).

The gneissic foliation in the country rocks of the CGC is predominantly NNE-SSW-striking, with moderate to steep dips; its average orientation (weighted mean) is N21°E/70°WNW (Figure 2). Stretching and mineral lineations in the foliation plane, mainly related to the D_3 phase, are mostly gently plunging to the north, with an average orientation of N8°E/11°N (Figure 2). At the outcrop scale, there are many D_3 -related isoclinal folds with their axial plane and axis respectively parallel to the foliation and lineation (Figure 4a) and also locally sheath folds elongated parallel to the lineation. Deformation in the migmatitic gneisses is highly heterogeneous and localized along several strike-slip shear zones concordant with the gneissic foliation and corresponding to D_3 structures. From one locality to another, shear criteria indicate either sinistral or dextral sense of movement (Figures 4b and 4c). We have identified, in particular, a NNE-SSW-trending, steeply-dipping sinistral shear zone, hereafter called the Camarat–Taillat Shear Zone (CTSZ), between the Camarat Cape and Taillat Cape bodies to the east, and the Escalet and Tourraque bodies to the west (Figure 2).

The western contact of the Camarat Cape body, well exposed at several places, is intrusive and underlined by swarms of a few centimeters to 2–3 m thick granitic dykes cutting across the migmatites and locally connected to up to \sim 1-m-thick tabular bodies concordant with the gneissic foliation (Figure 3b). It is generally NNE-SSW-trending and steeply dipping, hence roughly concordant with the pattern of the gneissic foliation in the Camarat Cape area and with the CTSZ which borders the granitic body (Figure 2). The northern and southern contacts of the Tourraque body are, on the contrary, discordant on the ca. N-S-trending foliation of the gneisses. They correspond to brittle-ductile tectonic contacts, as best seen in the junction zone between the Escalet and Tourraque bodies which is crowded with dominantly ca. E-W fractures, commonly filled with quartz and disposed in anastomosing networks (Figure 3c). To the west, an abrupt transition toward the wall rocks suggests also a sharp discordant contact for the Tourraque body, either resulting from magmatic stoping or, more probably, corresponding to one of the numerous ca. N-S strike-slip shear zones which cut across the migmatitic gneisses (Figure 2). The western contacts of the Escalet and Taillat Cape bodies are probably intrusive.

Three rock types can be distinguished in the Camarat granite: a coarse-grained granite where biotite is more abundant than muscovite (hereafter “Bt granite”; Figure 3d) and two cordierite-bearing varieties where muscovite is dominating over biotite. One of the latter is coarse-grained (hereafter “Crd granite”) and the other one is a microgranite (hereafter “Crd microgranite”; Figure 3d). The Camarat Cape and Escalet bodies are predominantly made of the Bt granite. The Crd granite is concentrated in the Tourraque and Taillat Cape bodies, where it is associated with tens of meters thick, mostly WNW-ESE-trending dyke-like lenticular Crd microgranite bodies (only the largest ones are represented in Figure 2). The Crd microgranite forms also, in the Camarat Cape area, small irregular bodies (outcrops of several tens of square meters) with lobate contacts, surrounded by the Bt granite and locally injected by metric dyke-like intrusions of the latter (Figure 3d). Contact between the Crd microgranite and the Crd or Bt granite over the entire area is sharp, but generally irregular and underlined by a slight decrease of the microgranite grain size. All these structural relationships between the different facies of the Camarat granite, in particular the occurrence of dyke-like bodies of one facies injected into another, testify to the coeval emplacement or almost so of magma batches with a quite high degree of crystallinity (crystal mushes).

Both the Bt and Crd granites contain magmatic enclaves, which consist of slightly elongated, decimetric mafic microgranular enclaves (MMEs) and very scarce, up to tens of meters large granodioritic enclaves, either porphyritic and very similar to the Gigaro granodiorite (Figure 3e) or fine-grained. Centimeter to meter thick aplite dykes occur sporadically (Figure 3e). They have an average orientation (weighted mean) of N88°E/80°S (Figure 2). In addition, the Camarat Cape body is crosscut locally by up to \sim 10-m-thick, steeply dipping and ca. E-W-trending dolerite dykes (not shown in Figure 2).

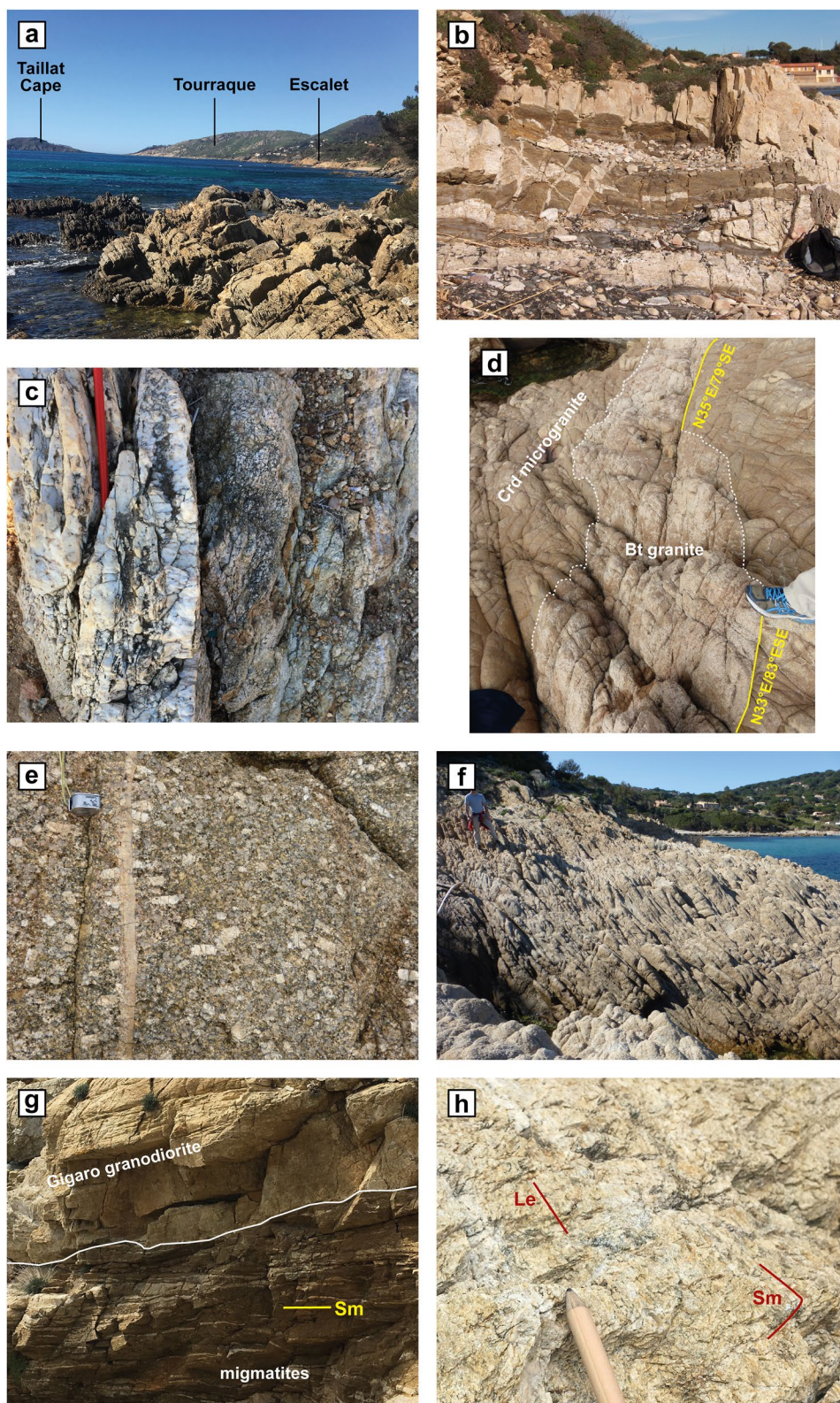


Figure 3.

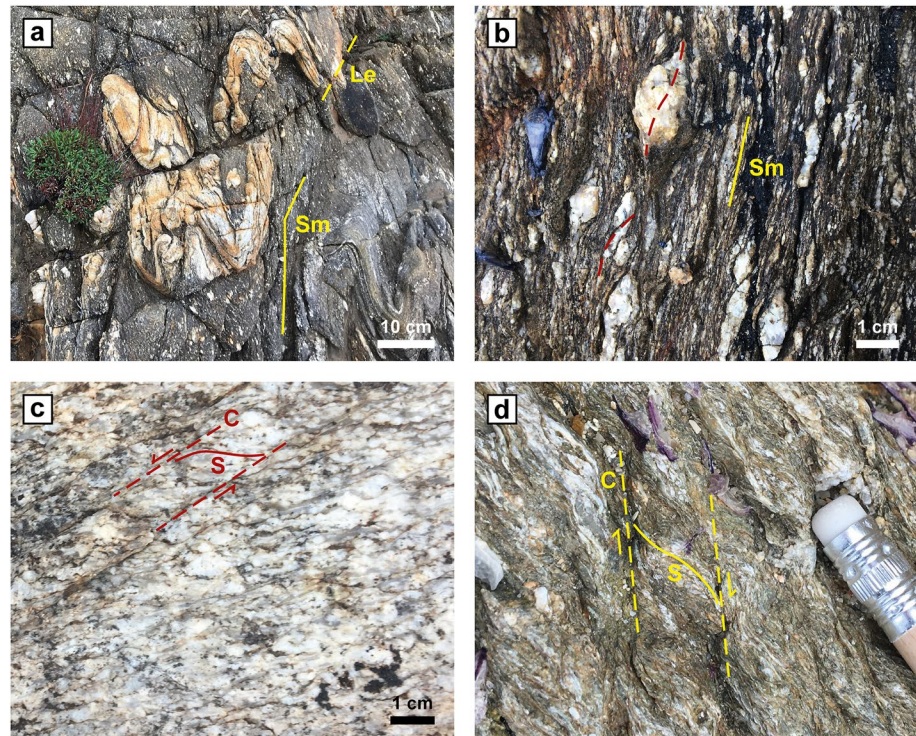


Figure 4. Field photographs of the migmatitic country rocks of the Camarat Granitic Complex. (a) D_3 -related isoclinal folds with axes parallel to the stretching lineation ($43^{\circ}12'21.19''N/06^{\circ}40'14.42''E$, looking north); (b) highly mylonitized migmatitic gneiss showing sinistral shearing ($43^{\circ}12'20.44''N/06^{\circ}40'14.67''E$, looking down from above); (c) S/C structure in a granitic vein demonstrating dextral shearing ($43^{\circ}11'04.02''N/06^{\circ}36'40.18''E$, looking down from above); (d) ultramylonite at the western border of the Gigaro granodiorite, with a S/C fabric ($43^{\circ}11'02.07''N/06^{\circ}35'53.68''E$, looking down from above). L_c : stretching lineation; S_m : gneissic or mylonitic foliation.

The Camarat granite is affected by very regular sets of fractures (joints and, locally, microfaults), with a dm-scale spacing and moderate to, dominantly, steep dips (Figure 3f). We have recognized three main sets of such fractures (Figure 2): two sets are subvertical and, respectively, N-S- and NNE-SSW-trending on average, and a third set, largely prevalent, is predominantly WNW-ESE-trending and steeply dipping to the SSW. The average orientation (weighted mean) of the fracture system is $N98^{\circ}E/80^{\circ}S$, which is at 90° to the mean trend of the lineations in the migmatitic gneisses and also very close (10°) to the mean orientation of the aplite dykes (Figure 2). Accordingly, these fractures appear to be early structures which control locally the orientation of the walls of aplite dykes, as well as the contact between the Crd microgranite and Bt or Crd granite, in particular the margins of dyke-like bodies (Figure 3d).

Fractures may be filled with quartz and/or chlorite, especially in the tectonic contact zone between the Escalet and Tourraque bodies where there is an increase in the number of such fractures, underlining an important deformation gradient. Quartz grains oriented perpendicularly to the fracture walls, as observed in this area (Figure 3c), have an average orientation (weighted mean) of $N1^{\circ}E/7^{\circ}N$, concordant to the mean pole of the fracture system at the scale

Figure 3. Field photographs of the Camarat Granitic Complex. (a) Panoramic view of the Escalet, Tourraque and Taillat Cape bodies and the surrounding migmatitic gneiss outcrops (foreground) from the south of the Camarat Cape ($43^{\circ}11'44.10''N/06^{\circ}39'30.38''E$, looking SW); (b) swarm of dm- to m-scale granitic dykes cutting across the migmatitic gneisses close to the NW contact of the Camarat Cape body (the dykes are connected to a m-thick tabular body, visible in the upper part of the photograph, concordant with both the gneissic foliation and boudinaged foliated leucosomes; $43^{\circ}12'21.94''N/06^{\circ}40'11.02''E$, looking NW); (c) quartz veins cutting across the granite in the contact zone between the Escalet and Tourraque bodies (note elongation of the quartz grains perpendicular to fracture walls; $43^{\circ}10'53.55''N/06^{\circ}38'25.46''E$, looking west); (d) dyke-like body of Bt granite in the Crd microgranite (note the locally rectilinear, fracture-controlled contact; site CA6A; $43^{\circ}11'41.13''N/06^{\circ}39'50.37''E$, looking NNE); (e) porphyritic facies similar to the Gigaro granodiorite forming an enclave in the Bt granite of the Camarat Cape body (note the thin aplite dyke; ca. $43^{\circ}12'20''N/06^{\circ}40'18''E$, looking south); (f) closely spaced fractures cutting across the Escalet body (site CA4; $43^{\circ}11'05.62''N/06^{\circ}38'33.90''E$, looking NNE); (g) mylonitic contact between the Gigaro granodiorite and the surrounding migmatites ($43^{\circ}10'24.78''N/06^{\circ}36'23.65''E$, looking north); (h) mylonitized Gigaro granodiorite at the eastern contact with the surrounding migmatites ($43^{\circ}10'25.13''N/06^{\circ}36'22.15''E$, looking NNE). L_c : stretching lineation; S_m : mylonitic foliation.

of the whole granite (N8°E/10°N) (Figure 2). The presence of (abundant) chlorite in the fractures shows that they functioned at the brittle-ductile transition under greenschist-facies conditions. The CTSZ also suffered low-grade reactivation, as attested by local fracturation or brecciation with crystallization of quartz and abundant chlorite, in particular at the junction between the shear zone and the southern tectonic contact of the Tourraque body.

The eastern edge of the N-S-trending Gigaro granodiorite (Figure 2) is highly mylonitized at the contact with the migmatitic gneisses, which is moderately westward dipping (Figures 3g and 3h). Stretching lineation and shear criteria indicate a top-to-the-south, sinistral displacement. The western border, on the other hand, is marked by a subvertical shear zone, with a decametric ultramylonite corridor and a dextral sense of shearing (Figure 4d), corresponding to the southern end of the Grimaud–Joyeuse Fault.

3.2. Petrographical Analysis

3.2.1. Mineralogy and Microstructural Relationships

Optical microscope observations and a complementary SEM analysis, conducted on polished thin sections made from the AMS samples, indicate that the primary mineral assemblage in the three facies of the Camarat granite consists of quartz, alkali feldspar (microperthite with Carlsbad twinning, locally microcline), plagioclase (albite-oligoclase), biotite and muscovite, with zircon, monazite, apatite and oxides as accessory minerals. Andalusite is a scarce accessory mineral, associated with cordierite in the Crd granite and microgranite. The oxides are ilmenite, magnetite (observed in only one sample, Bt granite CA19) and rutile which forms swarms of minute elongated inclusions parallel to cleavage in biotite.

The Bt and Crd granites are both heterogranular (mean grain size in the range 2–9 mm), locally porphyritic with \lesssim 1-cm-large megacrysts of rounded quartz, as well as euhedral alkali feldspar and plagioclase, in a fine-grained matrix (0.5–1 mm). In the Crd microgranite, the microstructure ranges from strongly heterogranular (fine-grained areas associated with and locally cutting across a coarser-grained assemblage; Figure 5a) to porphyritic (equi- to heterogranular fine-grained matrix containing megacrysts of rounded quartz, as well as euhedral alkali feldspar, plagioclase, muscovite, biotite and cordierite). For both kinds of microstructures in the microgranite, the mean size of the two coexisting grain populations is 0.2–0.6 mm versus 1.5–3.5 mm.

A moderate to strong, deuteric to later alteration affects feldspars (sericitization and formation of secondary muscovite), biotite (pseudomorphic replacement by chlorite), cordierite (pinitization), andalusite (transformation into muscovite), ilmenite (oxidation into rutile and (ferro)pseudobrookite) and magnetite (martitization). In addition to this alteration, feldspars and quartz are commonly fractured, some microfractures being coated with secondary phyllosilicates (chlorite, sericite, prehnite) or filled with a very-fine grained quartzo-feldspathic assemblage. These microstructures echo, respectively, circulation of greenschist-facies fluids and local emplacement of aplite dykes along macrofractures as observed in the field.

The modal proportions of biotite (possibly chloritized) and muscovite (both primary and secondary) have been estimated at 3%–7% and 0%–2% (up to 5% for the most altered samples) in the Bt granite, 1%–5% and 2%–6% in the Crd granite, and 1%–4% and 2%–8% in the Crd microgranite. The two last facies contain up to 5% of cordierite (generally heavily pinitized). The proportions of sizable (>20 μ m) grains of primary and secondary oxides range from 0.001% to 0.035%, except in sample CA19 (0.118%, with grains of magnetite up to ~550–600 μ m, whereas in the other samples the maximum size of the oxides is ~100–300 μ m).

3.2.2. Evidence of Ductile Deformation and Recovery

While the granite fabric is nearly isotropic, there is evidence of widespread, but weak straining at the microscale. First of all, most quartz grains display either an undulose extinction of variable intensity or an irregular pattern of subgrains (Figure 5b), pointing to ductile deformation and recovery. Locally, one finds also aggregates of small quartz grains interpreted as new grains developed by dynamic recrystallization (Figure 5c), probably made predominantly through subgrain rotation since the new grains are about the same size as neighboring subgrains (Passchier & Trouw, 2005; Stipp et al., 2002). The quartz-quartz boundaries, including in the aggregates of new grains, are commonly serrated (Figure 5d), indicating low-temperature grain boundary migration (bulging; e.g., Stipp et al., 2002). The bulges, however, only rarely evolved into new grains (bulging dynamic recrystallization). Quartz has therefore recorded a continuum of ductile deformation from medium temperatures, 400–500°C (subgrain rotation recrystallization) down to low-grade conditions, 300–400°C (bulging) (Stipp et al., 2002). Other microscale evidence of weak ductile deformation consists of a slight bending or kinking of (a)

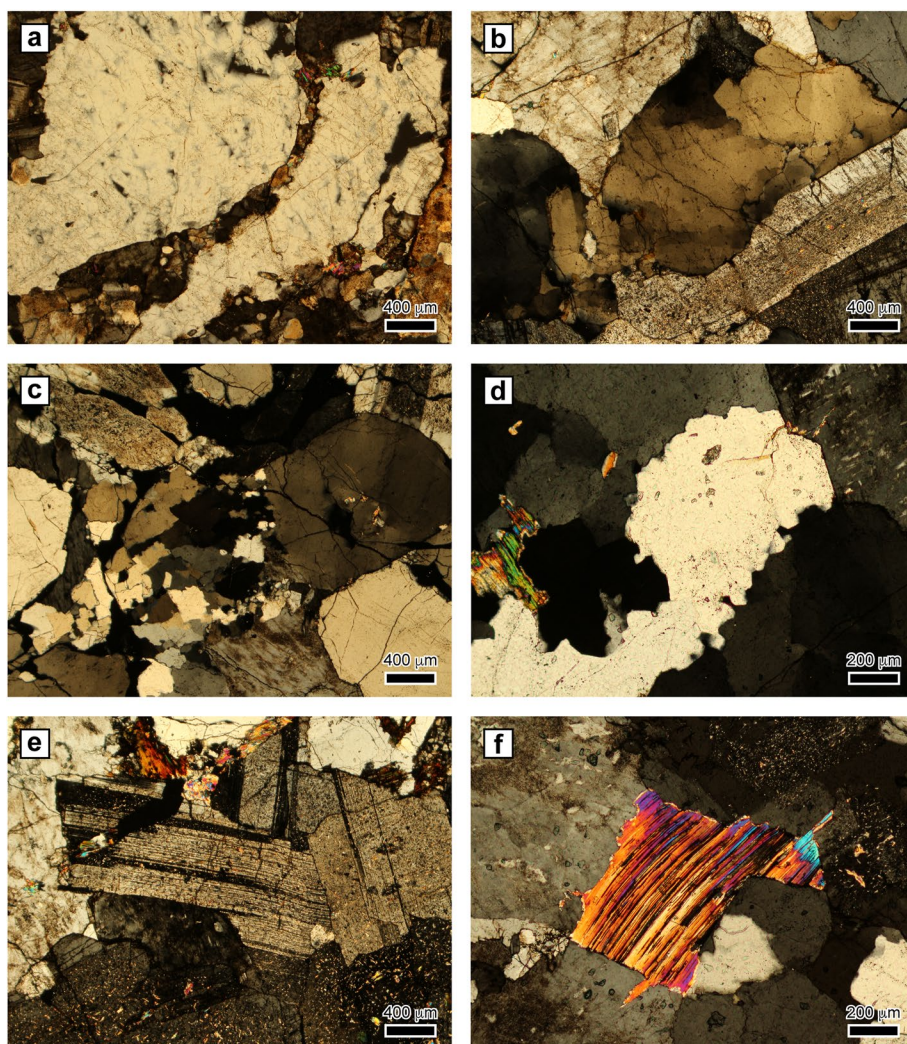


Figure 5. Microstructures in the Camarat granite (photomicrographs taken in transmitted light, with crossed polars). (a) Large grain of quartz cut by a finer-grained quartzo-feldspathic assemblage (sample CA16, Crd microgranite); (b) polygonized quartz grains displaying an irregular pattern of subgrains (CA18, Bt granite); (c) aggregate of small grains of quartz probably resulting from dynamic recrystallization (CA08, Crd granite); (d) serrated boundaries between quartz grains indicating bulging (note the more regular quartz vs. micropertthite boundaries in the upper right corner of the micrograph; CA20, Bt granite); (e) incipient kinking of a plagioclase crystal (CA18, Bt granite); (f) slight bending of the cleavage in a muscovite grain (CA09, Crd microgranite).

polysynthetic twins in plagioclase (Figure 5e), difficult to observe because of the sericitization, and (b) cleavage in biotite and muscovite (Figure 5f).

4. The Late Dykes

Late dykes from the MTM Internal Zone are particularly well exposed along the coast section to the NNE of the CGC, between the Pinet Cape and the Capon Tip (Pinet–Capon section; PCS in Figure 1b). There, they appear in the form of felsic dykes associated with some dolerite or composite dykes in which dolerite and fine-grained leucogranite are mingled (Duchesne et al., 2013). These dykes are centimetric to metric in scale and crosscut at high angle the main structural and magmatic structures associated with the D_3 phase, which is indicative of their late emplacement. However, some dykes are apparently undeformed, while others are folded and/or affected by the S_3 foliation (Figures 6a and 6b), suggesting a syn- to late-emplacement during the D_3 transpressive tectonic phase.

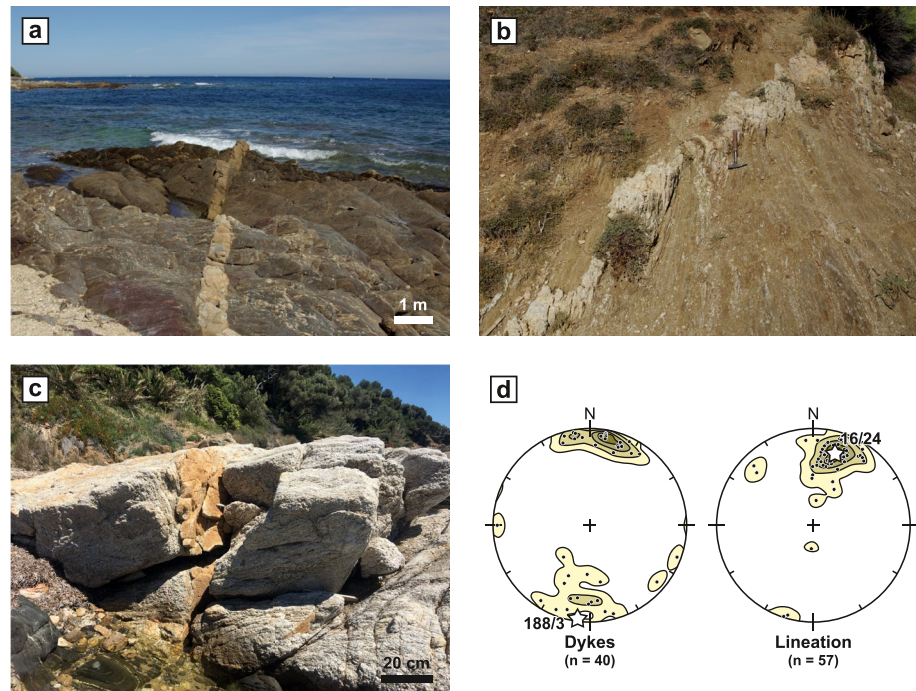


Figure 6. The Pinet–Capon section: field photographs of felsic dykes and structural data. (a) Fine-grained leucogranitic dyke (orientation N85°E/80°S) cutting across the S_3 foliation (N20°E/80°W) of the migmatitic gneisses (Capon Tip; 43°14′55.30″N/06°40′53.48″E, looking east); (b) fine-grained leucogranitic dyke (orientation N72°E/78°S) deformed by the S_3 foliation (N23°E/84°E) (Capon Tip; 43°14′55.45″N/06°40′53.60″E, looking NNE); (c) pegmatitic leucogranitic tabular body (sample MA04-02A), foliated and concordant with the S_3 foliation (orientation N20°E/70°E), crosscut by an aplitic leucogranitic dyke (sample MA04-02B) orientated at N120°E/75°S (Pinet Cape; 43°14′43.65″N/06°40′20.62″E, looking east); (d) equal-area plots (lower hemispheres) displaying poles of dykes (including four dolerite and five composite dykes from Duchesne et al. (2013)) and D_3 stretching lineations in the migmatitic gneisses (contours at 1–4–8–12% for the dykes and 1–5–10–15–20% for the lineations; white star: weighted mean).

The dykes are predominantly E–W-trending, with steep dips to the south or moderate to steep dips to the north, and have an average orientation (weighted mean) of N98°E/87°N (Figure 6d). According to Duchesne et al. (2013), the steepest dykes would be pure tension dykes perpendicular to the regional stretching direction, whereas the few less inclined dykes would be oblique to this direction, corresponding either to tension-shear dykes, equivalent to normal faults, or to passive dykes controlled by preexisting fractures. The weighted mean calculated for D_3 lineations in the migmatitic gneisses along the same coast section is N16°E/24°NNE (Figure 6d). On average, the Pinet–Capon dykes and the D_3 stretching direction recorded in their host rocks are therefore striking at $\sim 90^\circ$ from each other (the deviation is only 8°), which confirms the syn- to late- D_3 , pure tension or normal tension-shear nature of the dykes.

5. Material and Methods

Accurate description of the fabric of a granitic pluton through AMS measurements requires a sampling grid as regular as possible, the standard density of this grid being one site/km² (Bouchez, 2000). The small size of the Camarat granite (total outcrop ~ 3 km²) allowed us to use an even denser grid, with 20 sampling stations, that is, ~ 7 sites/km² (Figure 2). Twenty-one samples, named according to the corresponding sites (CA01 to CA20) were taken, with two samples coming from the same station, CA06 (samples labeled CA06A and CA06B). Ten samples (CA01 to CA05, CA06A,B, CA07, CA08, CA11) consist of a pair of one-inch oriented cores collected with a portable drill and further cut into 22 mm-high cylinders (four cylinders/sample). The 11 other samples (CA09, CA10, CA12 to CA20) are oriented blocks from which 21.5 mm-large cubes were extracted (3–7 cubes/sample). Anisotropy of magnetic susceptibility measurements were conducted on the small cylinders and cubes, respectively 40 and 48 specimens, using a low-field Kappabridge susceptometer.

Image analysis was carried out on mutually perpendicular sections cut across 10 out of the 11 oriented blocks (sample CA14, too weathered, was not investigated). Contrary to AMS which is an indirect technique for rock

fabric characterization, IA enables direct textural quantification. In the present study, it was used to characterize the shape fabric of the mafic minerals, to complete the AMS measurements and to confirm they can be used as a proxy of the petrofabric orientation, especially since many samples contain cordierite, a mineral with an inverse intrinsic magnetic anisotropy that is a potential source for anomalous AMS-derived magnetic fabrics (Amice, 1990).

Measurements of magnetic susceptibility versus temperature curves were performed on crushed offcuts from a selection of four blocky samples representative of the various facies of the Camarat granite and whose susceptibilities cover the range of susceptibility values calculated from AMS: CA12 (Crd granite from the Tourraque body), CA13 (Crd microgranite from the Taillat Cape body), and CA17, CA19 (Bt granite from the Camarat Cape body). Such thermomagnetic experiments enable to identify the contribution of ferromagnetic and paramagnetic minerals to susceptibility, a crucial prerequisite for the interpretation of AMS data.

Zircon and monazite grains separated from crushed portions of three blocks have been analyzed by LA-ICP-MS for U-Pb dating. Two of these blocks are CA13 and CA17 from the Camarat granite, dated to determine the emplacement age of the pluton. The third block is a non-oriented sample collected, for geochronological purpose only, in the eastern mylonitized facies of the Gigaro granodiorite (CA21; Figure 2).

Two samples were selected in the Pinet Cape area to constrain the emplacement age of the late dykes through muscovite $^{40}\text{Ar}/^{39}\text{Ar}$ geochronology. They originated from the same outcrop, where structural relationships are clearly identified (Figure 6c). Sample MA04-02A is from a foliated, coarse-grained leucogranitic tabular body (pegmatitic texture) parallel to the main S_3 foliation. Sample MA04-02B comes from an apparently undeformed, fine-grained leucogranitic dyke (aplitic texture) which crosscuts the main S_3 foliation and the pegmatitic leucogranitic tabular body.

All analytical methods are detailed in Supporting Information S1.

6. Results

6.1. Zircon and Monazite U-Pb Dating

6.1.1. Sample CA13

Zircons from sample CA13 (Crd microgranite from the Taillat Cape body; $43^\circ 10' 08.31''\text{N}/06^\circ 38' 44.88''\text{E}$) are euhedral, generally short-prismatic (aspect ratios from 1 to 3) grains mostly ranging in size from 75 to 150 μm . Most of them show medium to dark cathodoluminescence (CL) with regular oscillatory zoning, although some grains contain patchy zoned, CL-bright cores and/or very CL-dark rims (Figure 7a).

One zircon grain yielded two sub-concordant core analyses (spots #15 and #17) with a weighted mean Paleoproterozoic $^{207}\text{Pb}/^{206}\text{Pb}$ date of $1,840 \pm 10$ Ma and a rim analysis with a Devonian $^{206}\text{Pb}/^{238}\text{U}$ date of 376 ± 14 Ma (spot #16) (Figures 7a and 8a). Besides this grain, interpreted as inherited, that is, xenocrystic or restitic from the source rock, all zircons yielded younger $^{206}\text{Pb}/^{238}\text{U}$ dates. Out of 25 analyses on these grains, 16 show strongly discordant and highly scattered U-Pb data, with $^{206}\text{Pb}/^{238}\text{U}$ dates generally <300 Ma (Figure 8a). The remaining 9 analyses define a rough mixing line between radiogenic and initial Pb, with the four least discordant analyses carrying $^{206}\text{Pb}/^{238}\text{U}$ dates of about 300 Ma (Figure 8a). When anchored at the initial $^{207}\text{Pb}/^{206}\text{Pb}$ composition at this age (from Stacey and Kramers, 1975), these analyses yield a lower intercept date of 299.8 ± 6.0 Ma (MSWD = 2.6; $n = 9$) (Figure 8a).

Monazites from this sample show weak to no zoning in CL images, apart from a few grains displaying growth or patchy zoning (Figure 7a). The analyses yielded much more concordant and clustered U-Pb isotopic data than zircon. With the exception of 6 analyses showing discordance owing to the presence of initial Pb or slightly older $^{206}\text{Pb}/^{238}\text{U}$ dates, all analyses show identical $^{206}\text{Pb}/^{238}\text{U}$ and $^{207}\text{Pb}/^{206}\text{Pb}$ dates within uncertainty and define a Concordia date of 303.5 ± 4.0 Ma (MSWD = 0.9; $n = 16$) (Figure 8b). This date is within uncertainties identical to the lower intercept zircon date obtained from deemed magmatic zircons.

6.1.2. Sample CA17

Sample CA17 (Bt granite from the Camarat Cape body; $43^\circ 12' 13.02''\text{N}/06^\circ 40' 36.35''\text{E}$) contains euhedral, short-to long-prismatic crystals of zircon (aspect ratios from 2 to 5) mainly ranging in size from 100 to 250 μm . They all

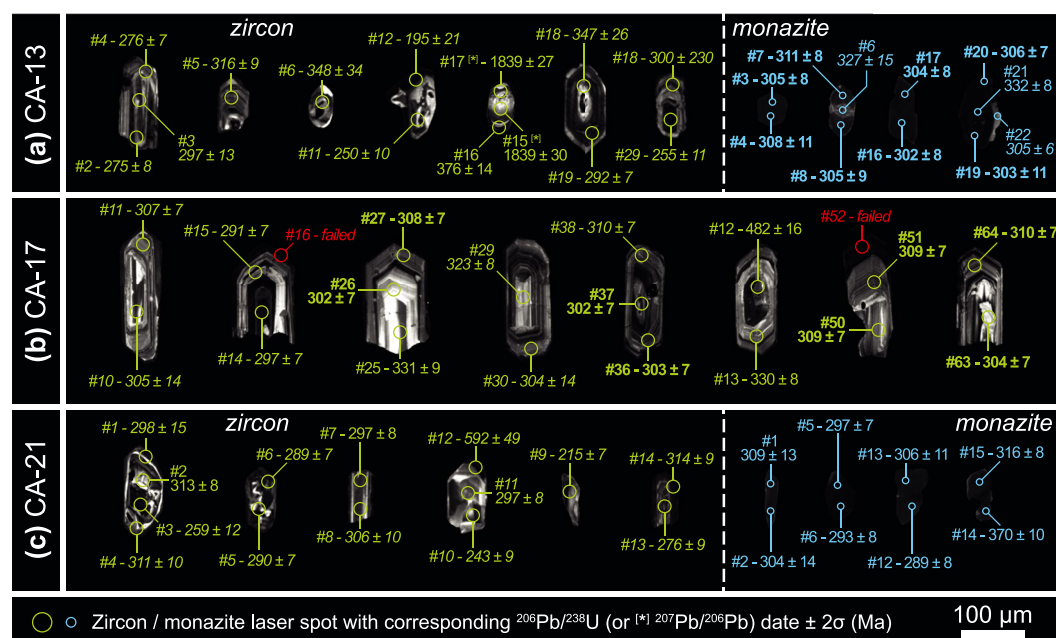


Figure 7. Representative cathodoluminescence images of zircon and monazite from samples of the Camarat Granitic Complex investigated here for U-Pb dating, that is, CA13 (a), CA17 (b), and CA21 (c). Laser spots with corresponding U-Pb dates are reported. Italic font indicates discordant U-Pb analyses; bold font indicates spots used in the calculation of Concordia dates (see Figure 8 and text).

show well-developed oscillatory zoning, usually with CL response varying from bright to dark from core to rim, although rare grains show the opposite or very little to no variation (Figure 7b). Some exhibit a dark-CL, partly resorbed or rounded core (Figure 7b).

All U-Pb analyses from such dark-CL cores are markedly discordant, except one yielding a $^{206}\text{Pb}/^{238}\text{U}$ date of 482 ± 16 Ma (spot #12) (Figures 7a and 8a), indicating that they likely correspond to inherited zircon. All analyses from oscillatory zoned domains are younger than 350 Ma; a few show concordant U-Pb dates in the range 340–320 Ma (notably from bright-CL cores). Besides these, more than half of the analyzed points in the sample ($n = 37$) define a trend likely corresponding to mixing between initial and radiogenic Pb and corresponding to a lower intercept date of 303.0 ± 3.1 Ma (MSWD = 1.3; Figure 8c). Using only the concordant data points from this population, a within uncertainty identical Concordia date of 304.5 ± 3.3 Ma (MSWD = 1.1; $n = 19$) is obtained (Figure 8d).

6.1.3. Sample CA21

Sample CA21 (mylonitized Gigaro granodiorite; $43^{\circ}10'25.03''\text{N}/06^{\circ}36'22.17''\text{E}$) yielded only few zircons: only 6 grains (Figure 7c) could be analyzed for U-Pb isotopes. The grains range from euhedral to subhedral, with lengths of 80–200 μm and aspect ratios from 2 to 4. They show patchy to oscillatory zoning and medium-gray CL response, with rare bright cores or growth zones (Figure 7c).

With the exception of two analyses (spots #2 and #7 with $^{206}\text{Pb}/^{238}\text{U}$ dates of 313 ± 8 and 297 ± 8 Ma, respectively), all obtained U-Pb data are discordant. Nevertheless, 8 analyses show $^{206}\text{Pb}/^{238}\text{U}$ dates clustered around 300 Ma and define a discordant trend pointing to the composition of initial Pb, along which plots another strongly discordant analysis (spot #12) (Figure 8e). Altogether, these 9 data points yield a lower intercept date of 293.2 ± 4.6 Ma (MSWD = 2.0) when anchored at the composition of initial Pb at 300 Ma (Figure 8e).

This sample also contains unzoned monazite grains (Figure 7c). Out of 17 U-Pb isotopic analyses on monazite, 12 are concordant but show a spread of significantly different $^{206}\text{Pb}/^{238}\text{U}$ dates over >40 Ma, between 321 ± 8 Ma and 281 ± 7 Ma (Figure 8f). These dates vary not only from grain to another, but also inside a single grain. A Kernel Density Estimate of this population shows a probability peak at ~ 295 Ma, overlapping with the zircon lower intercept date (Figure 8f).

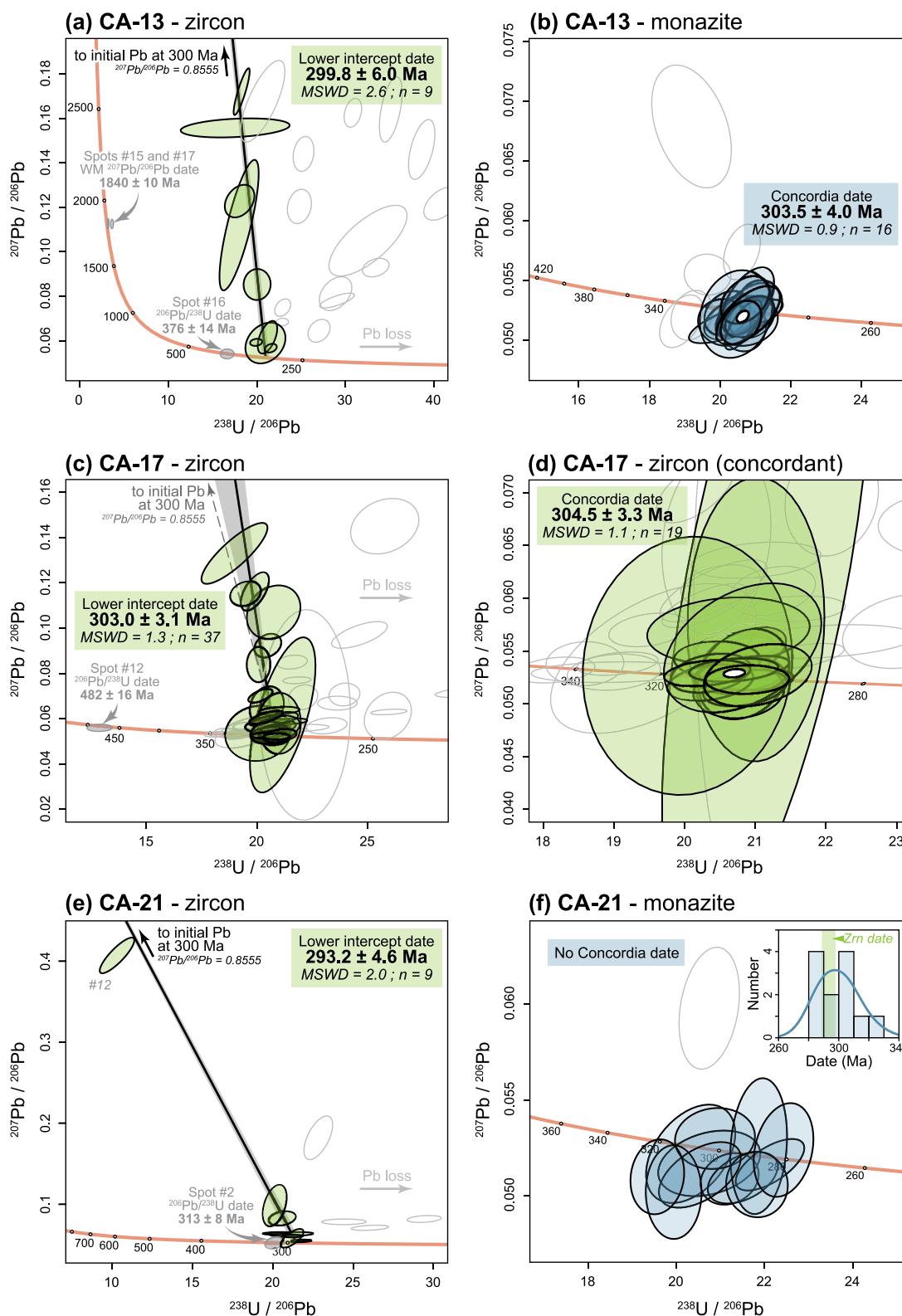


Figure 8.

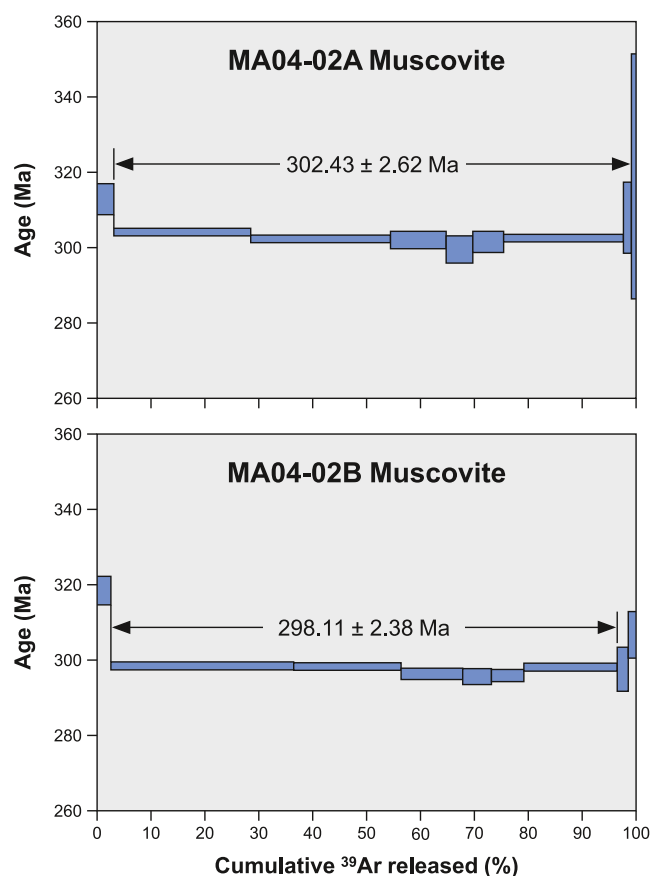


Figure 9. $^{40}\text{Ar}/^{39}\text{Ar}$ age spectra as a function of ^{39}Ar released on muscovite single grains from felsic dykes of the Pinet Cape area. The error boxes of each step are at the 2σ level. The error of ages is given at the 2σ level.

6.2. Muscovite Ar/Ar Geochronology

Sample MA04-02A ($43^{\circ}14'43.65''\text{N}/06^{\circ}40'20.62''\text{E}$). A single muscovite grain yielded a weighted plateau age of 302.43 ± 2.62 Ma, which corresponds to 96.43% of ^{39}Ar released and to seven steps (Figure 9). The inverse isochron for the plateau steps provides a concordant age at 301.07 ± 2.97 (MSWD = 1.25; initial $^{40}\text{Ar}/^{36}\text{Ar}$ ratio of 333.2 ± 37.1 Ma).

Sample MA04-02B (same coordinates as MA04-02A). A single muscovite grain yielded a weighted plateau age of 298.11 ± 2.38 Ma, which corresponds to 94.03% of ^{39}Ar released and to 6 steps (Figure 9). The inverse isochron for the plateau steps provides a concordant age at 297.62 ± 3.11 Ma (MSWD = 4.95; initial $^{40}\text{Ar}/^{36}\text{Ar}$ ratio of 334.1 ± 137.7 Ma).

6.3. Thermomagnetic Analysis

In the high-T heating curves of samples CA12, CA17, and CA19 (Figure 10), there is a Curie point at $557\text{--}570^{\circ}\text{C}$, indicative of a Ti-poor titanomagnetite, near end member magnetite in composition (3.6–1.4 mol% of ulvöspinel; Table 1). A well-defined Hopkinson peak preceding the susceptibility drop indicates the occurrence of single-domain (SD; $\leq 0.1\text{ }\mu\text{m}$) and/or small pseudo-single-domain (PSD; a few μm) individuals in the population of titanomagnetite grains (Dunlop, 2014; Dunlop & Özdemir, 2015). The high-T heating curve of CA13 exhibits also a Curie transition in the interval $550\text{--}580^{\circ}\text{C}$ (Table 1), however with no Hopkinson peak. We note also a susceptibility rise at a temperature of about -161°C in the low-T curve of CA19 (Verwey transition), indicating a larger amount of magnetite in this sample (probably with a PSD and/or multi-domain [MD] size; Clark, 1997), in agreement with higher values of the normalized susceptibility (Figure 10). Above the Curie transition, susceptibility still decreases with temperature in the high-T heating curves, as best seen for samples CA12 and CA13. This behavior is due to a titanohematite close to pure hematite (1.6–2.6 mol% of ilmenite; Table 1), as demonstrated by a small susceptibility drop at, respectively, 666°C and 657°C for the two last samples (Néel point; hardly visible in Figure 10).

The thermomagnetic curves show that magnetite does not only occur in sample CA19, as seen in polished thin sections, but is also present in the other samples, in even lesser amounts and probably with a lower mean grain size. These magnetite grains not revealed by the microscope analysis possibly occur as inclusions in biotite (Dunlop et al., 2006; Trindade et al., 2001). The almost pure hematite phase evidenced in the high-T heating curves corresponds to a secondary product left after alteration of magnetite, as seen in sample CA19, and also possibly ilmenite. It is tentatively assumed that the altered ilmenite hosts a secondary hematite not detected optically, since oxidation of ilmenite generally produces (titano)hematite in addition to rutile and (ferro)pseudo-brookite (e.g., Haggerty, 1991).

We have estimated the contribution to susceptibility of the ferromagnetic minerals (mostly magnetite in samples CA17 and CA19; magnetite plus some hematite in CA12 and CA13; Figure 10), using the iterative procedure of Richter & van der Pluijm (1994), as applied to the low-T curves and the fitting method of Hrouda (1994), as applied to the initial part of the high-T heating curves (Table 1). The two techniques give concordant results for samples CA17 (45%) and CA19 (75% vs. 77%), whereas the outcomes are very different or even aberrant for

Figure 8. Results of LA-ICP-MS U-Pb isotopic analyses of zircon and monazite from samples of the Camarat Granitic Complex, displayed in Tera-Wasserburg ($^{207}\text{Pb}/^{206}\text{Pb}$ vs. $^{238}\text{U}/^{206}\text{Pb}$) diagrams. Ellipses represent data points with uncertainties at 95% (2σ) confidence level. Light gray ellipses are excluded from the calculation of U-Pb dates; color filled ellipses are notable analyses discussed in text. In (a and e), the Discordia trends are anchored to the composition of initial Pb at 300 Ma due to the small number of analyses and/or their limited spread; in (c) the trend toward the latter is indicated as a dashed arrow. In (f) the inset shows a histogram and Kernel Density Estimate (blue curve) of concordant monazite $^{206}\text{Pb}/^{238}\text{U}$ dates in sample CA21. All uncertainties on calculated U-Pb dates include propagated systematic uncertainties (see analytical procedure in Supporting Information S1 for details).

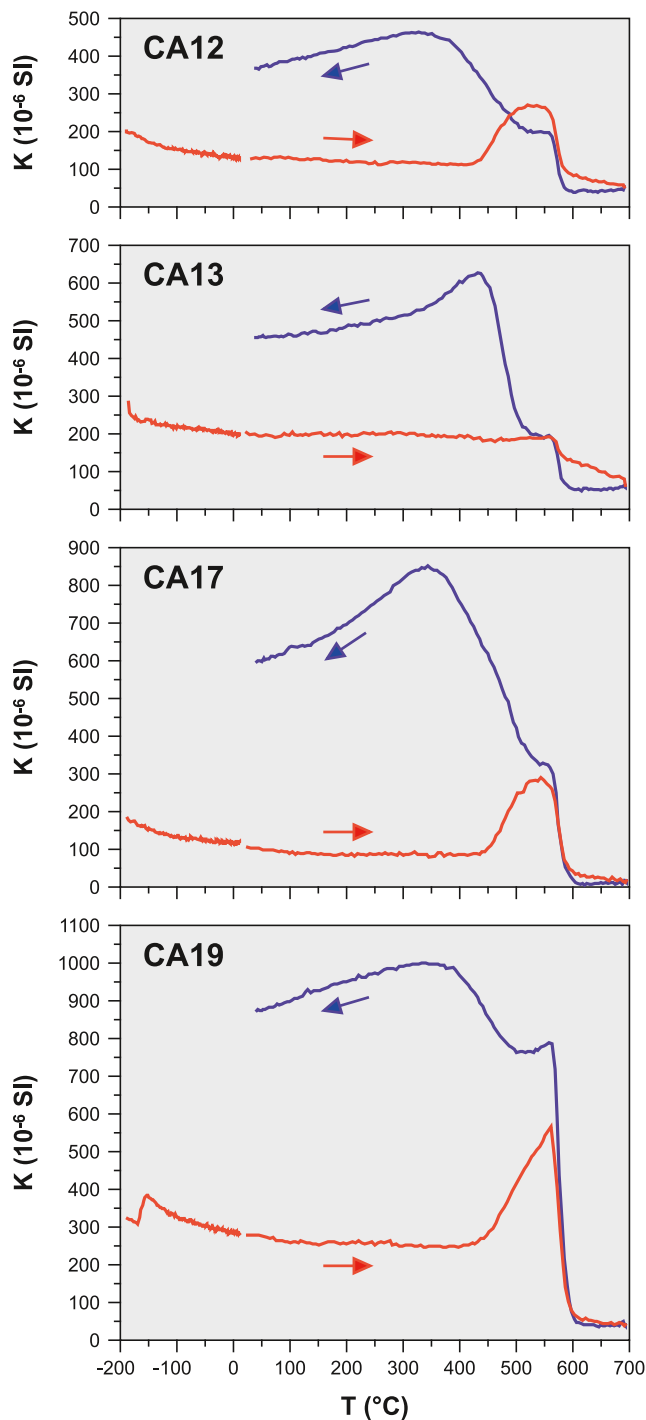


Figure 10. Magnetic susceptibility versus temperature curves. For each experiment, susceptibility measurements were normalized based on the volume (see Supporting Information S1).

generally heavily altered, with only scarce relicts subsisting within pinitized grains. The paramagnetic susceptibility component is thus carried mostly by biotite, and to a much lesser extent by primary and secondary muscovite, as well as other secondary minerals such as chlorite. The mean K_m value of the Bt granite ($65.4 \pm 17.3 \times 10^{-6}$ SI, excluding sample CA19 [$n = 8$]) is higher than that of the Crd microgranite and granite which are not significantly different from each other (respectively, $32.5 \pm 5.4 \times 10^{-6}$ [$n = 5$] and $38.1 \pm 6.2 \times 10^{-6}$ [$n = 7$]),

CA12 (40% vs. 76%) and CA13 (66% vs. 107%). Actually, both methods fail for the case of hematite bearing rocks (Hrouda et al., 1997; Richter & van der Pluijm, 1994). Therefore, for CA12 and CA13, the results only mean that the ferromagnetic contribution to susceptibility is not negligible.

The high-T cooling curves show a conspicuous increase in susceptibility (Figure 10), reflecting the formation of ferromagnetic Fe oxides during heating of the samples (Henry et al., 2003). A Curie point at 556–578°C indicates a secondary Ti-poor titanomagnetite closer to pure magnetite (3.6–0.0 mol% of ulvospinel) than the primary one (Table 1), coming from the breakdown of the Fe-Mg silicates. The Curie transition is followed by a small plateau or a minor Hopkinson peak (sample CA19), before a huge “hump” peaking at ca. 325–345°C or ~430°C (sample CA13) [(titano)magnetite to (titano)maghemite conversion?].

6.4. Anisotropy of Magnetic Susceptibility and Image Analysis

The output of the AMS measurements is an ellipsoid, whose principal axes are classically labeled $K_1 \geq K_2 \geq K_3$, that can be used to represent the magnetic fabric associated with the AMS. Similarly, IA provides an ellipsoid that characterizes a given shape subfabric, here the shape fabric of the mafic minerals. In the present study, the long, intermediate and short axes of this shape ellipsoid are labeled λ_1 , λ_2 , and λ_3 , respectively.

Mean AMS and IA data are given and compared in Table 2. Raw data with Schmidt plots are provided, sample by sample, in Supplementary Table 6 for AMS and Supplementary Table 7 for IA provided at <https://doi.org/10.17632/jd8m75cbm.1>.

6.4.1. Bulk Magnetic Susceptibility

The bulk magnetic susceptibility, $K_m = (K_1 + K_2 + K_3)/3$, varies from 20.1 to 282.8×10^{-6} SI for the individual AMS specimens ($n = 88$), the sample mean values ranging from 23.2 to 99.7×10^{-6} SI ($n = 20$), with one outlier value of 266.4×10^{-6} SI for CA19 (Table 2; Figure 11a). These K_m values are lower than 500×10^{-6} SI, the cutoff point below which rock magnetic susceptibility is classically considered to be controlled by paramagnetic minerals (Bouchez, 2000; Rochette, 1987). However, the thermomagnetic data demonstrate that the ferromagnetic contribution to susceptibility is far to be negligible in our samples, being up to ~75% in CA19 which has the highest magnetite content and, accordingly, the highest mean K_m value. The paramagnetic minerals that may contribute here to susceptibility in addition to magnetite (+ secondary hematite in some samples) are biotite (unaltered or chloritized), as well as muscovite (primary and secondary) and cordierite, both ferri-ferrous according to Amenzou (1988), and Fe-Ti oxides [ilmenite, rutile (ferro)pseudobrookite]. The contribution of the paramagnetic oxides is negligible, since they are found in trace amounts, and that of muscovite and cordierite is obviously minor compared to biotite, given their lower iron content [wt. % FeOt is 2.16 ± 0.58 for muscovite ($n = 31$) and 6.25 ± 1.27 for cordierite ($n = 8$) versus 22.58 ± 0.81 for biotite ($n = 17$); as calculated using electron-microprobe analyses of Amenzou, 1988]. Moreover, cordierite is

Table 1
Thermomagnetic Data

Sample	K_m	T_V	T_C		Usp(%)		T_N	Ilm(%)	Ferro(%)	
		LTw	HTw	HTc	HTw	HTc	HTw	LTw	HTw	
CA12	38.8	–	557	562	3.6	2.7	666	1.6	(40) ^a	(76) ^a
CA13	34.6	–	(521) ^a	556	(9.6) ^a	3.6	657	2.6	(66) ^a	(107) ^a
CA17	57.3	–	569	576	1.5	0.3	–	–	45	45
CA19	266.4	–161	570	578	1.4	0.0	–	–	75	77

Note. K_m : magnitude of the bulk magnetic susceptibility (in 10^{-6} SI), from Table 2; T_V : temperature of the Verwey transition (in °C), estimated as corresponding to the highest value of the curve slope in the transition interval; T_C and Usp(%): Curie temperature (in °C) estimated using the method of Petrovský and Kapička (2006) and corresponding mole fraction of ulvospinel (in %) in titanomagnetite calculated after Clark (1997); T_N and Ilm(%): Néel temperature (in °C) estimated using the method of Petrovský and Kapička (2006) and corresponding mole fraction of ilmenite (in %) in titanohematite calculated after Clark (1997); Ferro(%): ferromagnetic contribution (in %) to the low-field magnetic susceptibility, as estimated from about −190°C or −150°C (sample CA19) to ~10°C using the iterative procedure of Richter and van der Pluijm (1994) and from room temperature to ~200°C through the fitting method of Hrouda (1994); LTw, HTw, and HTc: value for low- T (warming), high- T warming and high- T cooling curve, respectively.

^aUnreliable or aberrant value. This concerns T_C and Usp(%) for sample CA13, and Ferro(%) for CA12 and CA13.

which confirms that biotite is the main contributor to paramagnetic susceptibility and may also be taken as a confirmation that the few grains of magnetite evidenced through the thermomagnetic analysis occurs mostly as inclusions in biotite.

6.4.2. Strength and Shape Parameters

The strength of the magnetic fabric, as described by the corrected anisotropy degree P_j (Jelínek, 1981) is very low (Table 2; Figures 11a and 11b): P_j is lower than 1.07, with mean values ranging from 1.010 to 1.027 ($n = 20$) and a mean of 1.018 ± 0.005 (i.e., 1.8% of anisotropy on average) for almost all samples. Sample CA19 stands out from the data set, as for K_m , with a higher mean P_j value (1.060). P_j and K_m are therefore positively correlated for CA19, but there is no obvious relationship between the two parameters for the other samples (Figure 11a). The very low anisotropy degrees that are found here are typical of undeformed to weakly deformed “paramagnetic” granitoids (see, e.g., numerous examples amongst the Variscan granitoids from the Pyrenees, as recently reviewed by Porquet et al., 2017). The positive correlation between P_j and K_m , as observed for sample CA19, reflects the influence of the magnetite grains on the fabric strength (Bouchez, 2000). Shape fabrics of the mafic minerals are systematically stronger than the magnetic fabrics, with P_j values in the interval 1.040–1.117 ($n = 10$) and a mean of 1.079 ± 0.023 (i.e., 7.9% of anisotropy on average) (Table 2; Figure 11c).

The fabric prolateness or oblateness is described here using the shape parameter T_j (Jelínek, 1981), with $-1 \leq T_j < 0$ indicating prolate fabrics and $0 < T_j \leq 1$ oblate fabrics. The T_j values for both the magnetic and mafic shape fabrics are quite variable, but indicate predominantly moderately prolate to moderately strongly oblate shapes (Table 2; Figures 11b and 11c). For the magnetic fabric, the T_j values of the samples are in the interval -0.831 – 0.455 ($n = 21$), with a mean value of 0.149 ± 0.320 . For the mafic shape fabric, T_j varies from -0.303 to 0.639 ($n = 10$), with a mean value of 0.027 ± 0.313 . There is no correlation between T_j and P_j for both kinds of fabrics (Figures 11b and 11c).

It is safer to take the P_j and T_j parameters of the shape fabric as proxies for, respectively, the strength and shape of the petrofabric, since the eccentricity and shape of the magnetic ellipsoid may be strongly influenced by the mineralogy. In particular, both vary according to mineral proportions when more than one mineral species with coaxial fabrics and different intrinsic anisotropies and shapes contribute to AMS (Borradaile & Jackson, 2004; Rochette et al., 1992). This applies to the Camarat granite, where susceptibility is carried by several mineral species.

6.4.3. Directional Data

The K_1K_2 plane, perpendicular to the K_3 axis, defines a magnetic foliation and the K_1 axis represents a magnetic lineation. The $\lambda_1\lambda_2$ plane of the shape ellipsoid, perpendicular to the λ_3 axis, and the λ_1 axis define fabric elements referred here to as shape foliation and shape lineation, respectively.

Table 2
Anisotropy of Magnetic Susceptibility (AMS) and Image Analysis (IA) Data (Sample Mean Values)

Sample #	Lat(N)	Lng(E)	Rock facies	Data type	n	K_m	P_j	T_j	A			C		
									Dec/Inc	Conf	σ_1/σ_2	Dec/Inc	Conf	σ_1/σ_2
CA01	43°12'19.62"	06°40'16.11"	Bt granite	AMS	4	64.2	1.012	−0.198	40/25	0.94	27/5	137/13	0.94	24/16
CA02	43°11'32.42"	06°39'09.28"	Bt granite	AMS	4	68.1	1.010	−0.166	6/12	0.76	48/31	276/3	0.50	77/39
CA03	43°11'19.99"	06°38'57.98"	Bt granite	AMS	4	63.4	1.024	0.412	203/15	0.77	55/14	110/13	0.89	36/14
CA04	43°11'05.62"	06°38'33.90"	Crd(?) granite	AMS	4	30.5	1.014	−0.297	329/33	0.86	42/13	143/57	0.78	45/32
CA05	43°10'48.89"	06°38'25.68"	Crd granite	AMS	4	37.3	1.016	0.238	345/36	0.84	38/25	244/14	0.88	39/8
CA06A	43°11'41.13"	06°39'50.37"	Crd microgranite	AMS	4	36.2	1.023	0.314	31/22	0.86	43/12	206/68	0.89	38/8
CA06B	43°11'41.67"	06°39'49.95"	Bt granite	AMS	4	36.5	1.018	0.455	46/20	0.97	21/6	163/52	0.92	26/20
CA07	43°12'05.41"	06°40'23.92"	Bt granite	AMS	4	66.7	1.021	0.202	9/8	0.91	34/6	125/71	0.95	23/11
CA08	43°10'51.80"	06°38'10.88"	Crd granite	AMS	4	35.0	1.010	−0.168	341/23	0.93	28/11	157/67	0.84	42/21
CA09	43°10'45.12"	06°38'14.90"	Crd microgranite	AMS	4	32.9	1.020	0.262	11/28	0.89	38/11	143/52	0.89	33/19
				IA	—	—	1.040	0.090	46/12	—	43/17	244/77	—	31/16
				Δ	—	—	0.020	0.172	36	—	—	42	—	—
CA10	43°10'39.87"	06°38'18.90"	Crd microgranite	AMS	4	35.8	1.014	−0.831	28/14	0.94	26/9	286/40	0.55	84/3
				IA	—	—	1.095	−0.035	40/34	—	10/4	248/53	—	10/4
				Δ	—	—	0.081	0.796	23	—	—	29	—	—
CA11	43°10'44.11"	06°38'26.76"	Crd(?) granite	AMS	4	34.2	1.024	0.425	13/13	0.97	20/6	209/77	0.94	26/10
CA12	43°10'31.86"	06°38'27.41"	Crd granite	AMS	4	38.8	1.015	0.354	208/10	0.75	50/32	306/35	0.75	47/35
				IA	—	—	1.072	−0.282	24/9	—	17/10	259/74	—	25/10
				Δ	—	—	0.057	0.636	19	—	—	45	—	—
CA13	43°10'08.31"	06°38'44.88"	Crd microgranite	AMS	4	34.6	1.016	0.130	7/8	0.93	29/5	250/74	0.90	34/14
				IA	—	—	1.086	0.512	23/22	—	48/11	260/54	—	17/6
				Δ	—	—	0.070	0.382	21	—	—	20	—	—
CA14	43°10'51.78"	06°37'32.06"	Crd granite	AMS	4	49.9	1.021	0.109	25/32	0.92	32/6	262/42	0.90	37/7
CA15	43°10'56.06"	06°37'22.15"	Crd granite	AMS	3	40.8	1.027	0.245	302/35	0.99	13/4	55/30	0.97	18/1
				IA	—	—	1.053	0.639	249/63	—	65/20	62/27	—	25/19
				Δ	—	—	0.026	0.394	43	—	—	7	—	—
CA16	43°10'55.57"	06°37'46.35"	Crd microgranite	AMS	4	23.2	1.026	0.453	15/28	0.96	22/7	120/26	0.96	22/4
				IA	—	—	1.068	−0.093	3/18	—	19/5	115/50	—	12/8
				Δ	—	—	0.042	0.546	15	—	—	24	—	—
CA17	43°12'13.02"	06°40'36.35"	Bt granite	AMS	7	57.3	1.015	0.373	12/10	0.71	62/18	124/65	0.91	30/15
				IA	—	—	1.092	−0.038	15/19	—	7/4	130/51	—	12/4
				Δ	—	—	0.077	0.411	10	—	—	14	—	—
CA18	43°12'00.17"	06°40'51.37"	Bt granite	AMS	6	99.7	1.014	0.279	48/44	0.93	28/14	178/33	0.97	17/9
				IA	—	—	1.071	−0.106	21/32	—	16/7	139/37	—	19/7
				Δ	—	—	0.057	0.385	24	—	—	32	—	—
CA19	43°11'45.66"	06°40'32.78"	Bt granite	AMS	4	266.4	1.060	0.131	350/48	0.99	14/1	167/42	0.96	23/7
				IA	—	—	1.095	−0.117	22/5	—	14/5	115/30	—	13/8
				Δ	—	—	0.035	0.248	51	—	—	43	—	—
CA20	43°11'46.50"	06°40'11.84"	Bt granite	AMS	4	67.3	1.013	0.400	307/6	0.62	73/21	117/84	0.86	34/27

Table 2
Continued

Sample #	Lat(N)	Lng(E)	Rock facies	Data type	n	K_m	P_j	T_j	A			C		
									Dec/Inc	Conf	σ_1/σ_2	Dec/Inc	Conf	σ_1/σ_2
				IA	—	—	1.117	−0.303	5/24	—	13/4	232/57	—	20/8
				Δ	—	—	0.104	0.703	58	—	—	36	—	—

Note. Lat(N) and Lng(E): latitude (north) and longitude (east); n: number of specimens used in the AMS measurements; K_m : magnitude (in 10^{-6} SI) of the bulk magnetic susceptibility; P_j and T_j : Jelinek's (1981) anisotropy degree and shape parameter; A and C: long and short principal axis of the magnetic fabric (K_1 and K_3) and the shape fabric (λ_1 and λ_3); Dec/Inc: declination/inclination of the axes; Conf: 2σ confidence level (in %) of the axis measurement (AMS data only); σ_1/σ_2 : dimensions (in degrees) of the 2σ confidence cone expressing the scattering of individual axis measurements; Δ : difference (absolute value) between IA and AMS data.

The magnetic foliations are relatively regularly orientated in the Camarat Cape–Escalelet bodies and more dispersed in the Tourraque–Taillat Cape bodies (Figure 12a), with average orientations of, respectively, N58°E/35°NNW (weighted mean for individual, mostly Bt granite specimens; $n = 45$) and N86°E/19°N (weighted mean for individual, Crd granite and microgranite specimens; $n = 43$). The magnetic lineations are predominantly gently to moderately plunging to the north or NE (Figure 12a), with similar average orientations (weighted means of individual axes) in the Camarat Cape–Escalelet (N22°E/23°NNE; $n = 45$) and Tourraque–Taillat Cape (N3°E/23°N; $n = 43$) bodies.

We have calculated an integrated shape ellipsoid for the northern and southern parts of the granite, by recombining the 2D raw data of the analyzed samples (Figure 12a). The result highlights the concordance, at pluton scale,

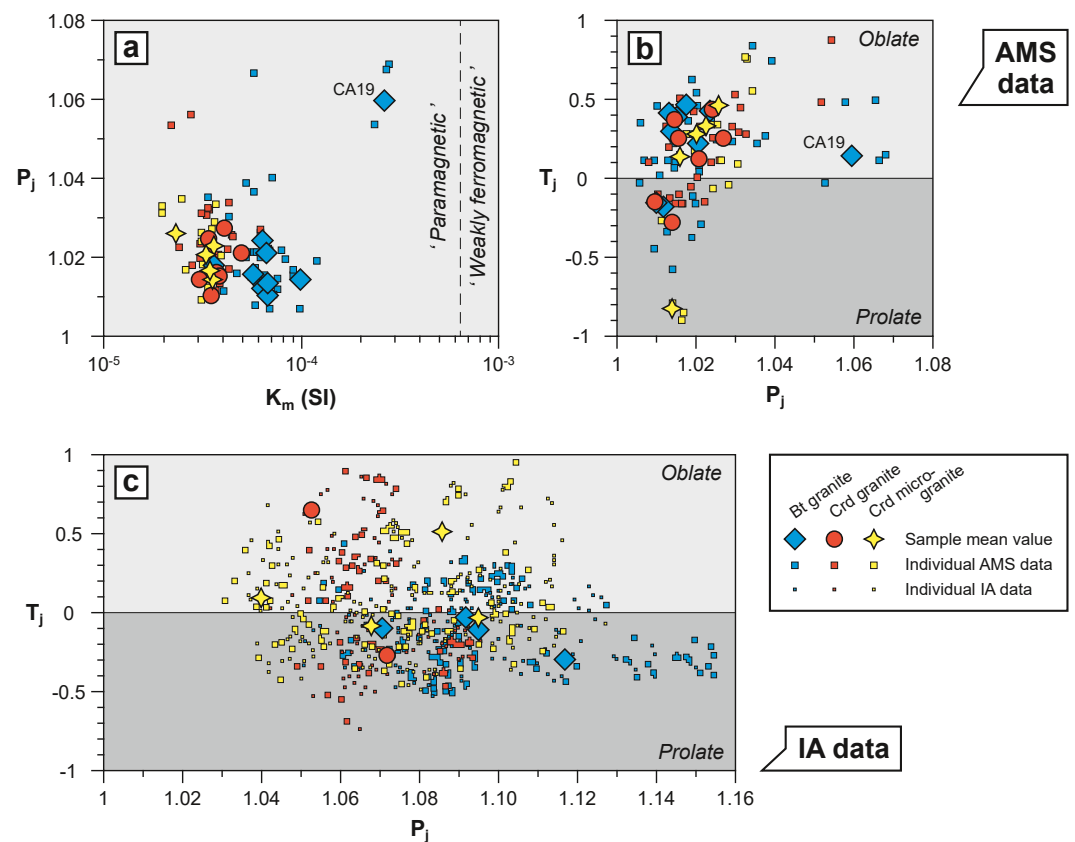


Figure 11. Scalar parameters K_m , P_j , and T_j for the magnetic and mafic shape fabrics. (a) Plot of P_j versus K_m ; (b) and (c) plots of T_j versus P_j . The individual anisotropy of magnetic susceptibility (AMS) data ($n = 88$) are those from the small specimens which were used to calculate the 21 mean magnetic ellipsoids (see text and Supplementary Table 6 provided at <https://doi.org/10.17632/jd8m75cbasm.1>). The individual image analysis (IA) data ($n = 640$) correspond to combinations of 2D raw data used in the reconstruction process of the 10 shape ellipsoids (64 combinations for each sample; see analytical procedure in the Supporting Information S1 and Supplementary Table 7 provided at <https://doi.org/10.17632/jd8m75cbasm.1>).

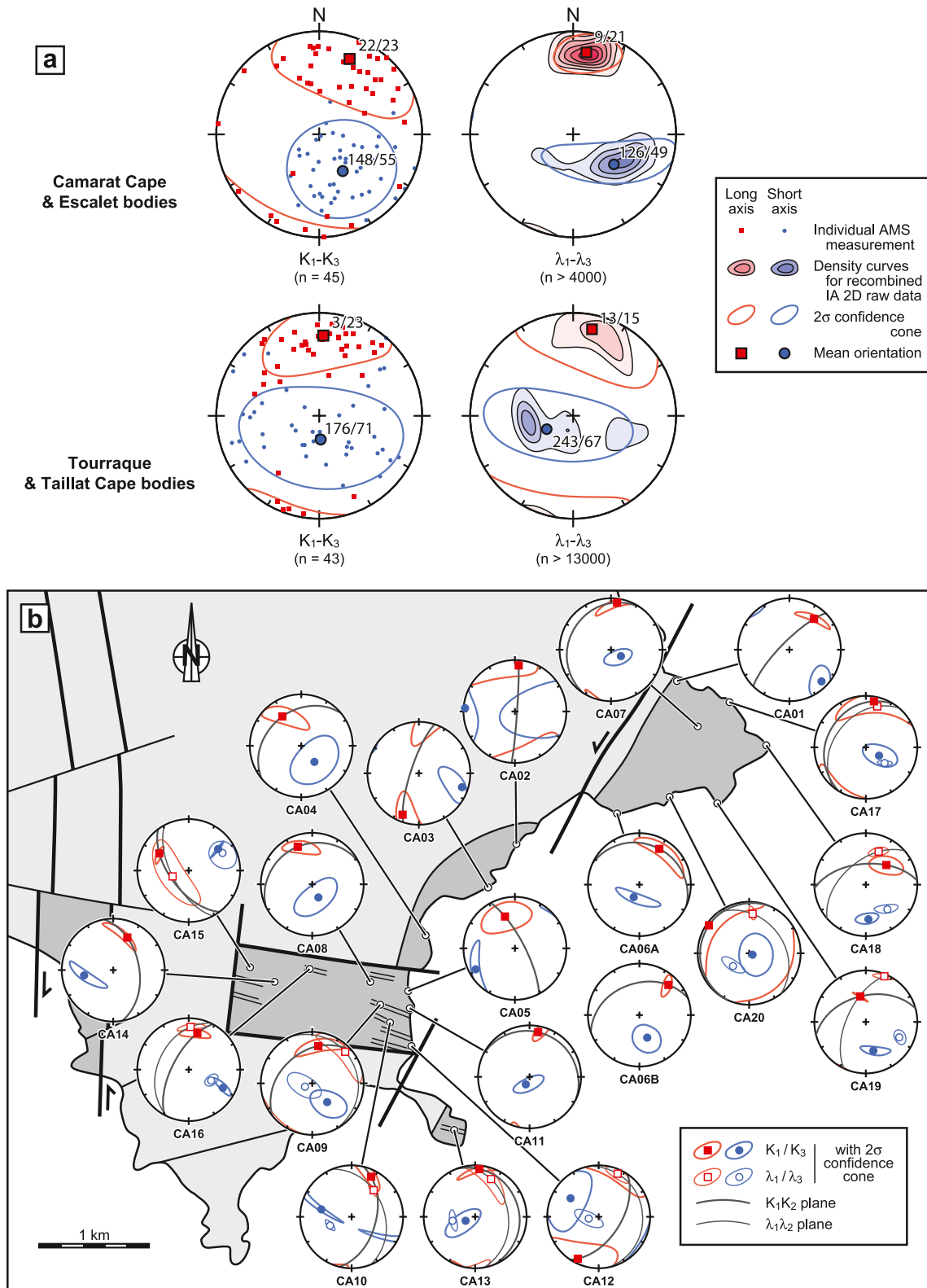


Figure 12. Directional data for the magnetic and mafic shape fabrics (lower hemisphere, equal-area plots). (a) Separately for the Camarat Cape–Escalet and Tourraque–Taillat Cape bodies, (1) K_1 – K_3 axes of the individual anisotropy of magnetic susceptibility (AMS) specimens ($n = 45$ and 43 , respectively), with average orientations (weighted means), and (2) contouring [contours at 6–9–12–15(–18–21)% and 6–9–(12)%, respectively] and averaging of λ_1 – λ_3 axes calculated through recombination of the image analysis (IA) 2D raw data (respectively, 4,096 combinations for four samples and 13,824 combinations for six samples; see text and Supporting Information S1); (b) site by site, mean K_1 – K_3 axes (and K_1K_2 planes), together with the λ_1 – λ_3 axes (and $\lambda_1\lambda_2$ planes) obtained by IA for 10 samples out of the 21.

between shape fabric of the mafic minerals and magnetic fabric, with average shape foliations and lineations at N36°E/41°NW and N9°E/21°N in the Camarat Cape–Escalet bodies (integrated means for four samples, CA17 to CA20; $n = 4,096$; 15° and 12° of angular deviation with the average magnetic foliation and lineation, respectively) and at N153°E/23°ENE and N13°E/15°NNE in the Tourraque–Taillat Cape bodies (integrated means for six samples, CA09-10, CA12-13, and CA15-16; $n = 13,824$; 23° and 12° of angular deviation with the average magnetic foliation and lineation, respectively).

A site-by-site comparison of the AMS and IA directional data (Table 2; Figure 12b) shows that, with a few exceptions, dispersion of the individual measurements around the mean axes is lower for the shape ellipsoids than for magnetic ellipsoids. The comparison also shows that at sample scale, (a) orientation of the shape foliations and lineations is a bit more homogeneous than that of the magnetic foliations and lineations, and (b) angular departures are from 7° to 45° (mean of 29°; $n = 10$) between shape and magnetic foliations, and from 10° to 58° (mean of 30°; $n = 10$) between shape and magnetic lineations.

It is suggested that the slightly higher variability in the orientation of the magnetic foliations and lineations reflects the occurrence of secondary minerals with no shape-/lattice-preferred orientation (SPO/LPO) or displaying a SPO/LPO not coaxial with that of the primary minerals controlling AMS. This also probably explains the higher uncertainty on the AMS measurements, at least partly. One of the most significant secondary minerals is probably hematite which contributes substantially to rock susceptibility in some samples, as revealed by the thermomagnetic data. It is also worth noting that the role of minerals with an inverse intrinsic anisotropy may be ruled out here. This concerns (a) cordierite (Amice, 1990) which, as already outlined above, only occurs as scarce relicts, strongly reducing its contribution to susceptibility, hence to the magnetic fabric, and (b) SD magnetite (Potter & Stephenson, 1988; and references therein) which is likely not abundant enough to affect significantly the magnetic fabric.

Foliation and lineation maps have been drawn by combining the AMS and IA data (Figure 13). For sampling sites where the two sets of data are available, the results with the best accuracy, that is, the less dispersed individual measurements, were selected. In case of similar dispersions of the measurements, the AMS data were preferred since the magnetic analysis concerns a larger number of grains than the direct textural quantification (for AMS, the analyzed rock volume varies from ~30 to ~70 cm³, depending on the sample, whereas IA uses 2D measurements of the SPO of grains made on three ~10 × 10 cm sections). The selected foliations have an average orientation (weighted mean) of N62°E/26°NNW and are organized around a roughly defined zone axis orientated at N9°E/21°N, subparallel (deviation of only 4°) to the weighted mean of the corresponding lineations (N13°E/21°NNE).

We observe a steepening of the foliations close to the western margin of the Camarat Cape body, which is concordant with the ca. N-S steeply dipping gneissic foliations and the similarly oriented CTSZ (Figure 13a). The foliations in the Escalet body are also steep and concordant with both the gneissic foliations and the CTSZ, at least close to the probable offshore extension of the latter. The foliation trajectories in the Tourraque body are dominantly at high angle with the gneissic structure of the country rocks. Moreover, they indistinctly crosscut the various facies of the Camarat granite, in particular the dyke-like bodies of Crd microgranite in the Tourraque body.

The lineations, which display a homogeneous pattern with a dominantly northerly shallow plunge, are concordant with the mostly D_3 -related lineations in the gneisses (Figure 13b). In places, in particular in the Tourraque body, lineation trajectories even cut across the granite margins. Accordingly, the mean lineation in the Camarat granite (N13°E/21°NNE) is very close (11°) to the mean lineation of the migmatitic gneisses in the area (N8°E/11°N; Figure 2). The lineation trajectories, as for the foliations, crosscut the internal contacts of the pluton.

7. Discussion

7.1. Geochronological Data

The results of zircon U-Pb dating revealed that in addition to a dominant population of late Carboniferous grains, samples CA13 and CA17 also contained zircon cores with pre-Carboniferous crystallization ages. A zircon core from sample CA13 yielded a ²⁰⁷Pb/²⁰⁶Pb age of $1,840 \pm 10$ Ma, reminiscent of already documented Proterozoic inherited zircons in the MTM, namely $1,930 \pm 28$ to $1,296 \pm 14$ Ma (Moussavou, 1998), ~1,003–1,010 and

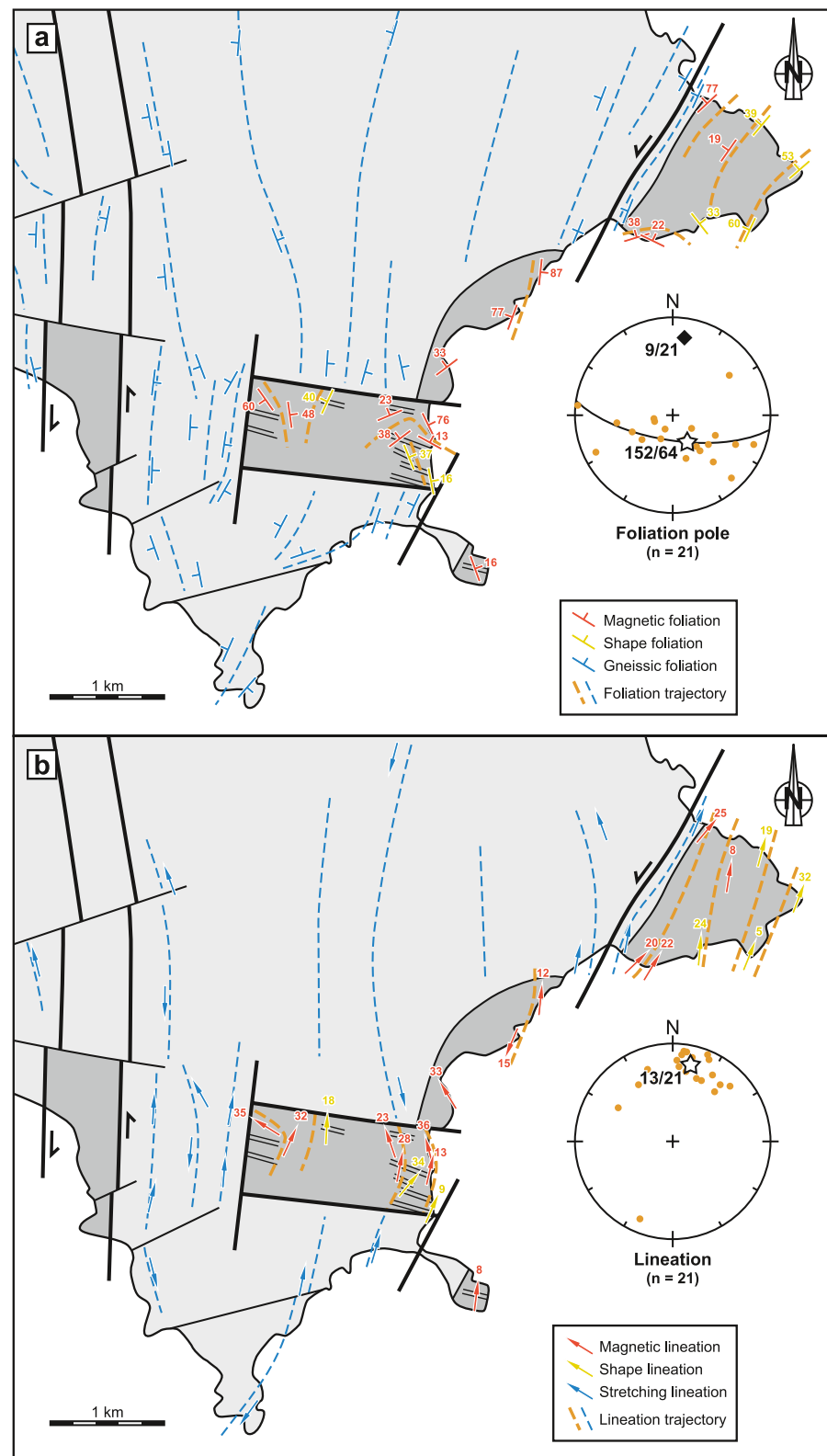


Figure 13. Composite map of the (a) foliations and (b) lineations in the Camarat granite, combining mean directional data from the magnetic and mafic shape fabrics. Structures in the country rocks are from Figure 2. Lower hemisphere, equal-area projections are also shown (white star, for both the foliations and lineations: weighted mean; great circle and black diamond, for the foliations only: best-fit girdle and its pole).

~1,800–2,500 Ma (Tabaud et al., 2022) in the Bormes orthogneiss, and $1,010 \pm 52$ Ma in the leucogranitic component of a composite dyke from the Pinet Cape located just to the east of the felsic dykes dated here by Ar/Ar geochronology (Duchesne et al., 2013). In other granitoids and orthogneisses of the Variscan realm, inherited Proterozoic zircons are generally interpreted as reflecting the incorporation of detrital zircons from metasedimentary source or surrounding rocks, rather than the presence of igneous crust of that age (e.g., Casti neiras et al., 2008; Laurent et al., 2017; Pereira et al., 2010; Schnapperelle et al., 2020). A similar interpretation is preferred here. Consistently, spectra of detrital zircon U-Pb ages found in Precambrian to early Palaeozoic sedimentary rocks from Peri-Gondwanan continental units extending from Central Iberia to China, and the adjacent Sahara Metacraton and Arabian–Nubian Shield (see compilations in Couzini  et al., 2019; and Stephan et al., 2019) show four main populations at 3.0–2.5 Ga, 2.1–1.7 Ga, ~1.0 Ga, and 800–550 Ma. The inherited zircons found in the MTM match the 2.1–1.7 Ga and the ~1.0 Ga populations.

The $^{206}\text{Pb}/^{238}\text{U}$ zircon date of 482 ± 16 Ma (sample CA17) is slightly older than zircon and monazite U-(Th-)Pb ages of ~455 to ~405 Ma obtained on a metabasite and calc-alkaline orthogneisses from the MTM Internal Zone, which date emplacement of oceanic subduction-related magmatic rocks, possibly followed by eclogitic metamorphism (M_0) (Demoux et al., 2008; Moussavou, 1998; Oliot et al., 2015). It falls, however, within the time span known for a widespread Ordovician arc-related magmatic event recognized in the Corso–Sardinian Block (~485–440 Ma; U-Pb zircon ages of the protoliths of calc-alkaline meta-igneous rocks; Casini et al., 2023; and references therein), which was followed by an early Devonian subduction-related HP metamorphism dated at ~420–400 Ma on mafic eclogites whose protoliths are penecontemporaneous with the calc-alkaline rocks (U-Pb zircon dating; references in Oliot et al., 2015). It falls also between ~505 and ~460 Ma, an interval of U-Pb dates obtained on overgrow rims of zircons from the Bormes orthogneiss, probably related to an Ordovician tectono-metamorphic event (Tabaud et al., 2022).

The $^{206}\text{Pb}/^{238}\text{U}$ date of 376 ± 14 Ma, as found in the rim of the Proterozoic zircon from sample CA13 and the dates in the range 340–320 Ma, as displayed by concordant zircons from sample CA17 may be ascribed to metamorphism or partial melting during the Variscan evolution of the MTM. Specifically, the former age correlates with the D1/M1 phase, lasting from ~380 to ~345 Ma, and the latter with the D2/M2 and D3/M3 phases, lasting from ~345 to ~325 Ma and ~325 to ~300 Ma, respectively, according to published monazite and zircon U-(Th-)Pb ages (Moussavou, 1998; Oliot et al., 2015; Simonetti et al., 2020), as well as amphibole, biotite and muscovite $^{40}\text{Ar}/^{39}\text{Ar}$ ages (Buscail, 2000; Corsini et al., 2010; Morillon et al., 2000), as discussed in Schneider et al. (2014) and Gerbault et al. (2018), and in the next section. These zircons thus likely represent xenocrysts from the country rocks sampled by the Camarat granite magmas upon ascent and emplacement.

The dominant population of youngest zircon and monazite dates of ~300–305 Ma, as found in samples CA13 and CA17 may reasonably be interpreted as emplacement ages of the granitic bodies. As already outlined above, for CA13, the zircon lower intercept date of 299.8 ± 6.0 Ma (MSWD = 2.6; $n = 9$) and the monazite Concordia date of 303.5 ± 4.0 Ma (MSWD = 0.9; $n = 16$) are identical within uncertainties. However, the latter is more precise and defined by only concordant dates. We retain therefore 303.5 ± 4.0 Ma as the best approximation of the emplacement age of the magmatic pulse represented by sample CA13 (Crd microgranite, Taillat Cape body). For CA17, we consider also the zircon Concordia date (304.5 ± 3.3 ; MSWD = 1.1; $n = 19$) as the emplacement age of the Bt granite in the Camarat Cape body. Although the zircon lower intercept date (303.0 ± 3.1 Ma; MSWD = 1.3; $n = 37$) is identical within uncertainties and calculated using more data points, many of them are indeed strongly discordant.

The ages of the Crd microgranite (303.5 ± 4.0 Ma) and the Bt granite (304.5 ± 3.3 Ma) are identical within uncertainties and considered to constrain emplacement and crystallization of the Camarat granite. These ages confirm and improve the precision of two previously published dates of 301 ± 10 Ma (Rb-Sr age on whole-rocks and alkali feldspars from the Camarat Cape and Tourraque bodies; Roubault et al., 1970, recalculated) and 298 ± 8 Ma (Rb-Sr age on whole rocks from the Camarat Cape and Escalet bodies; Amen zou, 1988). They are close to $^{39}\text{Ar}/^{40}\text{Ar}$ plateau ages of 300.2 ± 0.6 and 299.4 ± 0.6 Ma obtained by Morillon et al. (2000), respectively, on muscovite and biotite from one sample of the Camarat Cape body.

For sample CA21 (mylonitized Gigaro granodiorite), the two concordant zircon $^{206}\text{Pb}/^{238}\text{U}$ dates at 313 ± 8 and 297 ± 8 Ma fall within the interval of concordant monazite $^{206}\text{Pb}/^{238}\text{U}$ dates, from 321 ± 8 to 281 ± 7 Ma. Such a large spread of dates probably reflects disturbance of the U-Pb system during mylonitization, through recrystallization, fluid-assisted dissolution-precipitation, and/or crystallization of new zircon and monazite grains (Harlov et al., 2011; Langone et al., 2018; Wawrzenitz et al., 2012; Wayne & Sinha, 1988), and/or

the early Permian thermal anomaly, which is a regional-scale feature according to Casini, Cuccuru, Puccini, et al. (2015). In absence of any in situ geochronological data, it is not possible to discriminate between magmatic and deformation/fluid-related ages. In the same way, it is not easy to interpret the lower intercept date defined by the zircons (293.2 ± 4.6 Ma; MSWD = 2.0; $n = 9$), comparable to the monazite probability peak at ~ 295 Ma as already outlined above, which could be related to a younger event that affected the granodiorite (possibly the early Permian thermal peak). We note, however, that the monazite and zircon Concordia dates found for the Camarat granite fall within the interval of dates obtained for the mylonitized Gigaro granodiorite, which could indicate that emplacement of the Camarat granite is coeval with deformation of the Gigaro granodiorite. Conversely, this would indicate that the Gigaro granodiorite is potentially older than the Camarat granite, with the oldest dates obtained on both zircon (313 ± 8 Ma) and monazite (321 ± 8 Ma) providing minimum crystallization ages for the Gigaro granodiorite.

$^{39}\text{Ar}/^{40}\text{Ar}$ muscovite ages of 302.43 ± 2.62 Ma and 298.11 ± 2.38 Ma obtained, respectively, on a pegmatitic tabular body and on an aplitic dyke from the Pinet Cape area (samples MA04-02A and MA04-02B) are not significantly different from each other. The felsic component of the neighboring Pinet composite dyke has revealed a statistically undistinguishable U-Pb zircon date of 310 ± 10 Ma but, as discussed by the authors (Duchesne et al., 2013), this date corresponds to inherited zircon cores and instead of dyke emplacement, most probably dates the migmatitization of the host rocks. In the Tanneron Massif, a ca. E-W leucocratic dyke crosscutting the main N-S-trending D_3 tectonic structures (S_3 , L_3) of the Cannes–La–Bocca migmatitic orthogneiss yielded an U-Pb monazite date of 297.1 ± 4.9 Ma (Demoux et al., 2008), similar to the $^{39}\text{Ar}/^{40}\text{Ar}$ muscovite ages of our samples MA04-02A and MA04-02B. A late Pennsylvanian to earliest Permian age may therefore be retained for the late felsic dykes.

Collectively, previously published and new geochronological data argue in favor of a penecontemporaneous emplacement for the Camarat granite and the swarm of ca. E-W late dykes crosscutting the Internal Zone, most probably in a short period of time between ~ 305 and ~ 298 Ma. Dolerite dykes from this swarm are not dated, but at least some of them are also penecontemporaneous with the Camarat granite (dykes of this composition cutting across the Camarat Cape body have undulating margins, which suggests they were emplaced before complete crystallization of the granitic magma; Duchesne et al., 2013). The 301.8 ± 3.6 and 301 ± 2 Ma ages found, respectively, by Demoux et al. (2008) (monazite U-Pb dating) for the Rouet granite in the Tanneron Massif and by Duchesne et al. (2013) (zircon and monazite U-Pb dating) for the Moulin-Blanc leucogranite, a strongly foliated tiny body displayed along the coast to the east of St-Tropez (MBG in Figure 1b), fall within the same age interval. All these granites and dykes are witness to a thermal event that affected the MTM at the end of its late-Variscan evolution, in the context of a crustal hot zone according to Duchesne et al. (2013). The Plan-de-la-Tour granite, dated at 329 ± 3 Ma (monazite U-Th-Pb age; Oliot et al., 2015) and 324 ± 5 Ma (zircon U-Pb age; Moussavou, 1998), and potentially the Gigaro granodiorite (minimum ages of 313 ± 8 and 321 ± 8 Ma on zircon and monazite respectively; see above) represent slightly older magmatic pulses in that late evolution.

7.2. Tectonic Control of the CGC Emplacement

Fabric studies using the AMS technique, as conducted worldwide on granitoids from orogens of various ages repeatedly concluded that these granitoids are syntectonic despite they are generally nearly isotropic (Archanjo et al., 1994; Benn, 2010; Benn et al., 1998; Benn et al., 2001; Bolle et al., 2018; Bouchez et al., 1990; Gleizes et al., 1998; Gébelin et al., 2006; among many others). These syntectonic granitoids have in common to display signs of weak but widespread intracrystalline deformation and recovery, locally with dynamic recrystallization, as well as a fabric consistent with the regional pattern, such as lineations parallel to regional stretching directions and fold axes or fabric deflection by tectonic shearing. In agreement with these works, inconspicuous microstructural evidence of ductile deformation (Figure 5) and continuity of lineations across the intrusive contacts (Figure 13b), as observed here, testify to the emplacement of the Camarat granite in a regional tectonic strain field. The syntectonic nature of the granite is also supported by its association with main strike-slip shear zones, in particular the CTSZ toward which there is a steepening of the magmatic foliation (Figure 13a). It cannot be excluded, moreover, that the shear zones controlled the ascent and emplacement of the granitic magmas (Brown & Solar, 1998; Hutton, 1988; D'Lemos et al., 1992; Ferré et al., 1997; Gébelin et al., 2006). The E-W elongation of the Tourraque body and its termination against ca. N-S strike-slip shear zones to the east (CTSZ) and to the west, as well as the intercalation of ca. E-W-trending dyke-like bodies of Crd microgranite within the Crd granite in the area (Figure 2) further point to emplacement either in a pull-apart structure or in a large-scale, box-shaped tension fracture. The fabric of the Gigaro granodiorite was not studied here in details. However, location between

two shear-zones (Figure 2) suggests that the ascent and emplacement of this part of the CGC were also tectonically controlled. This agrees with the emplacement model of the Plan-de-la-Tour–Rouet granitic complex in a pull-apart domain, along the Grimaud–Joyeuse Fault, as proposed by Onézime et al. (1999).

It is also worth noting that the local concordance between fractures and either aplite dykes or dyke-like bodies in the Camarat granite (Figure 3d) suggests that the fracture system may have controlled, at least locally, emplacement of the latest magma batches, in a same deformation context. In addition, the presence of abundant chlorite associated with quartz in these fractures, as well as in the CTSZ points to significant fluid circulation related to the emplacement of the granitic magmas at rather shallow depths.

Agreement between the average orientation of the D_3 lineation from the migmatitic host rocks and the average orientations of the magmatic lineation, aplite dykes and fracture system from the Camarat granite, as well as the WNW-ESE trend of the Crd microgranite dyke-like bodies (Figures 2 and 13b) demonstrate that the Camarat granite has recorded, from its emplacement to cooling down to relatively low temperatures, the ca. N-S direction of maximum stretching of the D_3 phase. The D_3 lineations are subhorizontal and ca. N-S-trending not only in the vicinity of the granite, but also in the whole MTM Internal Zone where their strike falls in the interval $\sim N0^\circ$ – $15^\circ E$ (Corsini & Rolland, 2009). The orientation of the late dykes in the Internal Zone is also consistent with the D_3 ca. N-S stretching direction materialized by these lineations, as demonstrated by our structural data from the Pinet–Capon section (Figure 6d).

Since emplacement of the Camarat granite and associated late dykes is coeval with the D_3 tectonics, their crystallization age of ~ 305 – 298 Ma directly date the D_3 event. Other constraints on the D_3 timing come from the crystallization ages of: (a) the Plan-de-la-Tour–Rouet granitic complex (329 ± 3 Ma; Oliot et al., 2015; and 324 ± 5 Ma; Moussavou, 1998; for the Plan-de-la-Tour granite; 301.8 ± 3.6 Ma; Demoux et al., 2008; for the Rouet granite) that was emplaced along the Grimaud–Joyeuse Fault in a strike-slip context (Figure 1; Onézime et al., 1999), concomitantly with the D_3 transpressive shearing (Corsini et al., 2010; Schneider et al., 2014); and (b) the Moulin-Blanc leucogranite (301 ± 2 Ma; Duchesne et al., 2013) whose fabric mimics the structural pattern of the surrounding gneisses, as shaped by the D_3 phase. Furthermore, D_3 transpression has been recently dated at 327 ± 3 and 325 ± 5 Ma along the La Garde-Freinet–Cavalaire Fault using U-Th-Pb in situ monazite geochronology (Simonetti et al., 2020). In short, the present geochronological data and published U-(Th)-Pb ages collectively indicate that the D_3 event lasted from ~ 325 to ~ 298 Ma.

7.3. Transition of Strain Regime Near the Carboniferous–Permian Boundary

The stretching direction of the late Carboniferous–earliest Permian (D_3) transpressive phase and the extension direction of the (D_4) rifting phase which initiated in early Permian times also compare very well. According to Toutin-Morin and Bonijoly (1992) which have studied the Permian basins from the MTM area, focusing on the rift between the Maures and Tanneron massifs (Figure 1b), the Permian extensional tectonics was polyphasic with (a) a minor NNE-SSW extension phase leading to the formation of small basins to the east of the La Moure Fault (Argentièrre and Avellan basins; ArB and AvB in Figure 1b) and (b) a major N-S extension giving rise to the main basins between the Maures and Tanneron massifs (Bas-Argens and Estérel basins; BAB and EB), and other large basins further west (Le Luc and Toulon–Cuers basins; LLB and TCB). However, all the Permian grabens and normal faults are dominantly WNW-ESE in the focus area of Toutin-Morin and Bonijoly (1992)'s model (Figure 1b) and we consider therefore the D_4 event in that area as a single extensional phase characterized by a NNE-SSW direction of extension. This direction is parallel to the previous (D_3) lateral flow, as recorded in the Internal Zone, in particular in the Camarat granite.

Thus, the main evolution of the deformation regime between the D_3 and D_4 phases consisted in a progressive transition from transpression, associating folds, strike-slip shear zones and very localized transtension with small intramontane coal-bearing basins, to a regional extensional deformation in a same and persistent subhorizontal, ca. N-S direction of stretching. In this context, the coexistence of sinistral and dextral senses of shearing in the migmatitic gneisses (Figures 3b and 3c) argues for a pure shear dominated tectonic regime (Passchier & Trouw, 2005), at least in the late stages of D_3 and during the transition toward D_4 .

7.4. Comparison With Corsica and Sardinia

The Corso–Sardinian Block, overprinted by the Alpine collision in NE Corsica, was formerly closely facing the MTM, as demonstrated by a convincing body of evidence (references in Edel et al. (2014)). In the most widely accepted, late-Variscan palinspatic reconstruction of the area, the geological structures and the metamorphic zoning of the MTM and the Variscan basement of northern Sardinia are continuous (Figure 14a). In particular,

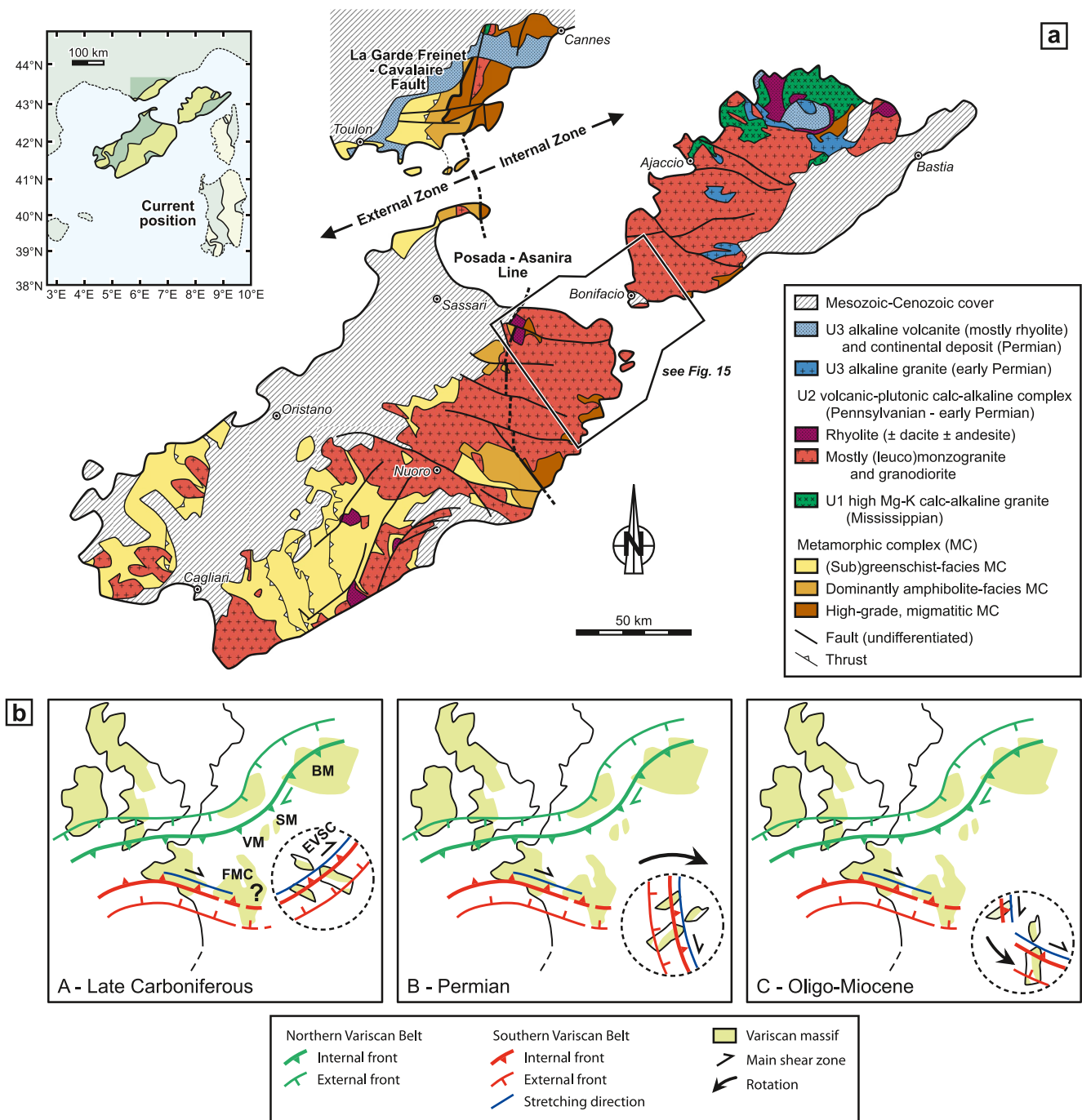


Figure 14. The SE European Variscan Belt. (a) Late Paleozoic palinspastic reconstruction, in present-day coordinates, highlighting the geological correlation between the Maures–Tanneron Massif and the Corso–Sardinian Block (from Edel et al. (2014) and Gueguen (1995)). The geological map of the Maures–Tanneron Massif is a simplified version of Figure 1. Geology of the Corso–Sardinian Block was simplified from Cocherie et al. (2005) for Corsica and Carnignani et al. (2016) for Sardinia, with additional information from Casini, Cuccuru, Puccini, et al. (2015), and modification from Orsini et al. (2011) and Casini, Cuccuru, Maino, et al. (2015) for S. Corsica and N. Sardinia, respectively, to fit with Figure 15a. (b) Paleogeographic evolution starting in early Permian times, that is, just after emplacement of the Camarat granite and showing the successive large-scale rotations that led to the current relative position of the Maures–Tanneron Massif and the Corso–Sardinian Block (from Edel et al. (2018) and Martínez Catalán et al. (2021)). BM, Bohemian Massif; EVSC, East Variscan Shear Zone; FMC, French Massif Central; SM, Scharzwald Massif; VM, Vosges Massif.

the Posada–Asinara Line in northern Sardinia (Cappelli et al., 1992; Carosi et al., 2012; Carosi & Palmeri, 2002) and the La Garde-Freinet–Cavalaire Fault in the MTM can be considered as two sections of the same large-scale high-strain zone which separates two main contrasted tectono-metamorphic domains (Simonetti et al., 2020). The Corso–Sardinian Block has been separated from the MTM in Oligo-Miocene times, during rifting and opening of the Liguro-Provençal back-arc oceanic basin (e.g., Jolivet et al., 2020), through a counterclockwise rotation of $\sim 50^\circ$ (30° for Corsica and 60° for Sardinia after Westphal et al. (1976); 55° for the two islands following Gueguen, 1995; 45° for Sardinia after Gattacceca et al. (2007); $\sim 50^\circ$ for the two islands when the mean trend of transversal faults is compared, as calculated in the present study).

Magmatism in the Variscan basement of Corsica and Sardinia is mostly represented by the Corsica–Sardinia Batholith, a 400-km-long versus 50-km-wide plutonic-volcanic province, elongated along a N-S direction (Figure 14a). Based on field relationships, as well as petrological and geochemical arguments, three main magmatic suites have been recognized in this batholith (e.g., Rossi & Cocherie, 1991). The earliest suite (U1), found only in NW Corsica, is defined by high-Mg-K calc-alkaline granites and subordinate ultrapotassic mafic rocks, emplaced between 347 and 328 Ma (Mississippian) (Li et al., 2014; Paquette et al., 2003). The second magmatic suite (U2) has emplacement ages in a large interval, ~ 320 –280 Ma (Pennsylvanian–early Permian) (Casini, Cuccuru, Maino, et al., 2015; Padovano et al., 2014; Paquette et al., 2003; Rossi et al., 2015). It encompasses calc-alkaline products with a lower Mg-K content, namely granitoids making up the bulk of the batholith and subordinate volcanic rocks (mostly early Permian rhyolites). The U2 granitoid suite has been further subdivided in Corsica into two successive components, U2a and U2b. The youngest magmatic suite (U3), well defined only in Corsica, is partly coeval with the U2 suite (290–278 Ma, i.e., early Permian) (Cocherie et al., 2005; Paquette et al., 2003; Renna et al., 2007; Rossi et al., 2015). It comprises A-type (per)alkaline granitoids and dominantly rhyolitic volcanic rocks, as well as (ultra) mafic complexes and related dykes. The ~ 335 Ma dominantly tonalitic intrusions and the ~ 325 –300 Ma granitoids (e.g., the Camarat granite) of the MTM are equivalent, respectively, to the U1 and U2 suites (Gerbault et al., 2018). The alkaline volcanism in the Permian grabens cutting and bordering the MTM is comparable to the U3 magmatism of Corsica (references in Durand, 2008). The progression from U1 to U2 and finally U3 recorded the evolution from a contractional to an extensional tectonic setting, through a transition from contraction to extension in a strike-slip-dominated regime (Casini, Cuccuru, Puccini, et al., 2015; Gerbault et al., 2018; Paquette et al., 2003).

We will focus here on AMS data acquired by Gattacceca et al. (2004) and Edel et al. (2014) on U2 (and possibly U3; Casini, Cuccuru, Puccini, et al., 2015) plutons of the Corsica–Sardinia Batholith in southernmost Corsica and northernmost Sardinia. The structure and magmatic evolution of the batholith in these two areas have been constrained recently by geological mapping, geochemical analyses and U-Pb zircon and monazite dating (Casini, Cuccuru, Maino, et al., 2015; Orsini et al., 2011) that may be coupled with other recent geochronological data (Casini et al., 2012; Padovano et al., 2014; Oggiano et al., 2014, 2015; and references in Casini, Cuccuru, Maino, et al., 2015). Two groups of intrusions have been identified, their equivalence from one area to another (S. Corsica vs. N. Sardinia) being, however, not certain (Figure 15a). Intrusions of the first group (attributed to the U2a suite in S. Corsica) have a Pennsylvanian to early Permian age (~ 320 –290 Ma). Their dominant orientation is NW-SE to WNW-ESE and, in N. Sardinia, some of them occur as partly to completely foliated elongated bodies emplaced along or within strike-slip shear zones. Intrusions of the second group (U2b in S. Corsica) are early Permian in age (~ 290 –280 Ma). They have a NE-SW orientation in S. Corsica, and their counterparts in N. Sardinia form ca. E-W-trending igneous complexes. Contrasted modes of emplacement have been proposed for the two groups of granitoids: emplacement controlled by conjugate, NW-SE dextral and E-W sinistral strike-slip shear zones for the oldest group (>290 Ma), at least for several Sardinian intrusions (Casini et al., 2012) and emplacement within large-scale NE-SW tension fractures for the youngest group (<290 Ma), both in S. Corsica and N. Sardinia (Casini, Cuccuru, Maino, et al., 2015; Gattacceca et al., 2004). These interpretations were integrated by Casini, Cuccuru, Puccini, et al. (2015) into a model of geodynamic evolution of the Corso–Sardinian Block, which considers, for the U2 and U3 events, a progressive transition from (a) a 325–300 Ma (late Carboniferous) transpressive phase during which strike-slip shear zones channeled ascent and emplacement of crustal melts to (b) a 300–270 Ma (early Permian) extensional phase during which crustal melting produced magmas that were emplaced as shallow plutons and volcanic complexes in extensional domains equivalent to the Permian post-orogenic continental basins.

We have combined the AMS data of Gattacceca et al. (2004) and Edel et al. (2014) and calculated average (weighted mean) magnetic lineations for the two groups of granitoids (ages >290 Ma vs. <290 Ma) taking into account the recent works on S. Corsica and N. Sardinia, as described above (e.g. the data of Gattacceca et al. (2004) from the northernmost tip of Sardinia were interpreted by these authors “in a single block,” while

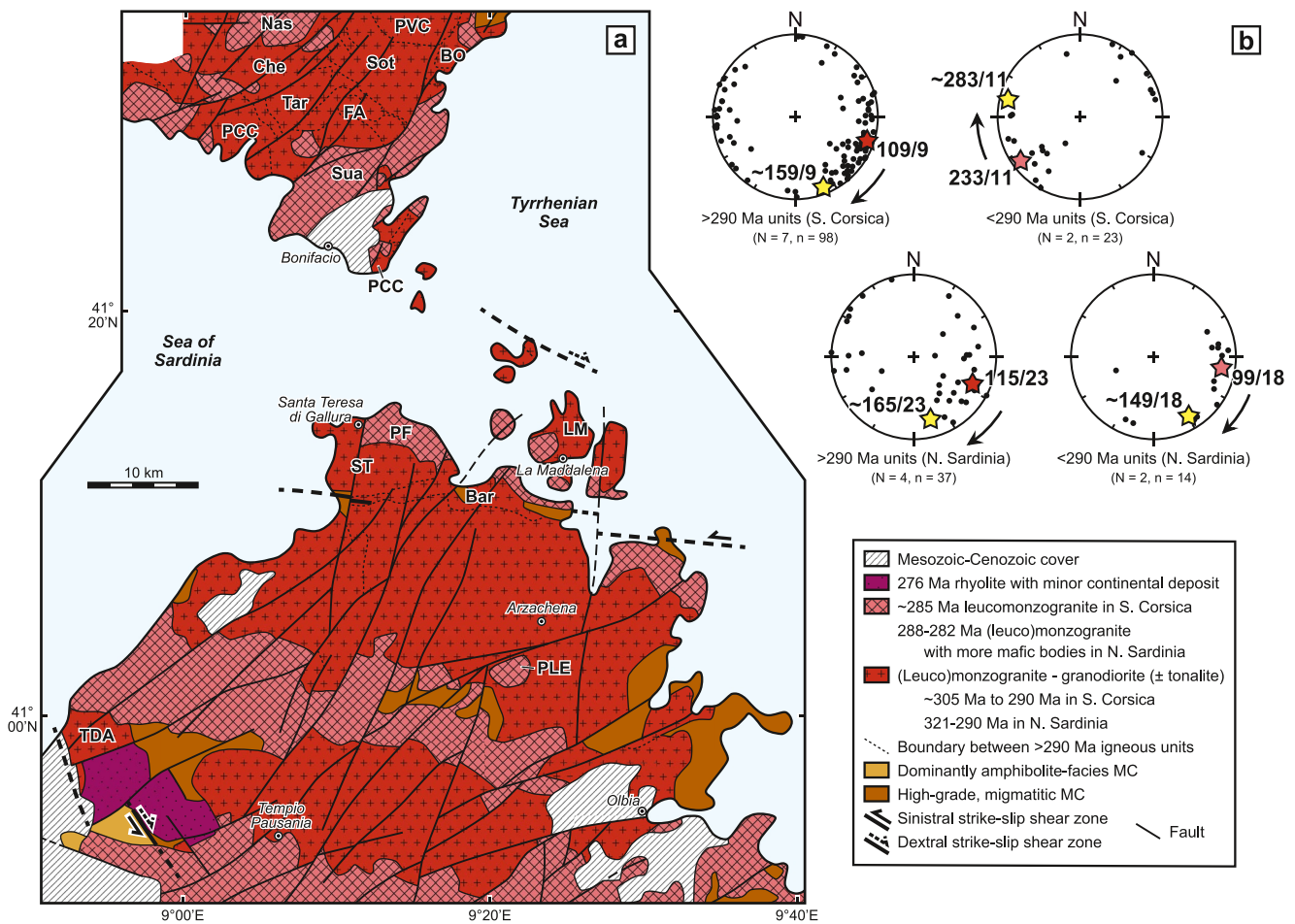


Figure 15. Anisotropy of magnetic susceptibility (AMS) data from late-Variscan granitoids of southernmost Corsica and northernmost Sardinia. (a) Geological map of the Corsica–Sardinia Batholith in S. Corsica and N. Sardinia, simplified from Orsini et al. (2011) and Casini, Cuccuru, Maino, et al. (2015), respectively (ages are U–Pb dates from references listed in the text). MC in the map legend stands for metamorphic complex (see Figure 14a). “Plutons” of interest in S. Corsica (more probably subunits of large plutons, by analogy with S. Sardinia), >290 Ma (“U2a”): BO, Bocca di l’Oru; Che, Chera; FA, Figari–Arapa; PCC, Pianotolli–Caldarelllo–Chevanu; PVC, Porto-Vecchio–Chitebbiu; Sot, Sotta; Tar, Tarabucceta; <290 Ma (“U2b”): Nas, Naseo; Sua, Suartone. Plutons in N. Sardinia, >290 Ma: Bar, Barrabisa; LM, La Maddalena; ST, Santa Teresa; TDA, Trinità d’Agultu; <290 Ma: PF, Punta Falcone; PLE, Punta La Ettica. (b) Equal-area plots (lower hemispheres) with mean magnetic lineations in the granitoids located in part (a) of the Figure (BO, Che, etc.), recalculated from AMS data of Gattacceca et al. (2004) and Edel et al. (2014). N, number of igneous units covered by the AMS data; n, number of AMS sites; red star, average lineation (weighted mean) in present-day coordinates; yellow star, id. after a clockwise rotation of $\sim 50^\circ$ to correct for rifting and opening of the Liguro-Provençal basin.

they cover actually three different units, two from the oldest group of intrusions and one from the youngest group). For the >290 Ma granitoids, the average magnetic lineation is gently plunging to the ESE, implying a dominantly subhorizontal, WNW-ESE stretching direction, ca. N–S if Corsica and Sardinia are rotated back into their late Paleozoic position (respectively, red and yellow stars in Figure 15b). These results agree with the predominance of WNW-ESE to NW-SE, gently plunging lineations measured in the field by Casini et al. (2012) in some of the oldest granitoids from N. Sardinia. For the <290 Ma granitoids, the average magnetic lineation has a similar orientation, but only in N. Sardinia (Figure 15b): in S. Corsica, the lineations are dominantly parallel to the well-defined NE–SW elongation of the plutons. According to Gattacceca et al. (2004), this peculiar orientation is due to the narrowness of the large-scale tension fractures into which the magmas were emplaced, these fractures being, however, roughly orthogonal to the stretching direction. It is also worth to note that some NE–SW magnetic lineations occur in the >290 Ma units, particularly in S. Corsica (Figure 15b).

The AMS data published for representatives of the Corsica–Sardinia Batholith from S. Corsica and N. Sardinia therefore suggest the persistence of the same stretching direction, ca. N–S in present-day coordinates, during the transition from late Carboniferous transpression to early Permian extension, as seen for the MTM. As for the MTM, this model is also supported by the orientation of dykes (not shown in Figures 14a and 15a). Swarms

of basaltic to rhyolitic, steeply dipping dykes are indeed widespread in the Corsica–Sardinia Batholith and its metamorphic basement. They are late Carboniferous to middle Triassic in age, the oldest dykes being products of the U2 and U3 magmatic events (Traversa et al., 2003). Dyke swarms are predominantly \sim N0–30°E-trending in S. Corsica (Orsini et al., 2011), as well as in N. Sardinia where this ca. N–S orientation rotates progressively southwards up to \sim N40°E (Carmignani et al., 2016). As already stressed by Gattacceca et al. (2004), such an orientation, NNE–SSW in average and the steep attitude of the dykes indicate a WNW–ESE, subhorizontal direction of opening, parallel to the average stretching direction revealed by the AMS data from the granitoids.

7.5. Significance at the Scale of the Southern European Variscan Belt

In the MTM and Corso–Sardinian Block, large-scale orogen-parallel ductile strike-slip shear zones were responsible for the exhumation of the orogenic crust in a transpressional context at \sim 325–300 Ma (Schneider et al., 2014; Gerbault et al., 2018 and references therein). As discussed by Simonetti et al. (2020), these strike-slip structures, the La Garde-Freinet–Cavalaire, Grimaud–Joyeuse and La Moure faults in the MTM, and the Posada–Asinara Line and other shear zones in the Corso–Sardinian Block, belong to the crustal-scale high-strain zone which affects the eastern segment of the SE Variscides (the East Variscan Shear Zone of Corsini & Rolland, 2009; EVSZ in Figure 14b). Sinistral ductile shear zones developed at first within amphibolite facies metamorphic conditions associated with partial melting, followed by dextral shear zones within brittle-ductile conditions (Carosi et al., 2012; Frassi et al., 2009; Giacomini et al., 2008). The progression from Devonian–early Carboniferous to early Permian reflects the evolution from a contractional to extensional tectonics in a strike-slip regime (Casini, Cuccuru, Puccini, et al., 2015; Gerbault et al., 2018). We show here that during this transition, a striking feature is the persistence of a ca. N–S stretching direction, which supports a strong horizontal crustal flow developed parallel to the orogen coeval with HT–LP metamorphic conditions and partial melting. This pattern is typical of transpressional zones particularly in ancient orogenic belts characterized by a hot, buoyant lithosphere (Cagnard et al., 2006; Duclaux et al., 2007; Pelletier et al., 2002).

According to the paleogeographic reconstructions of Domeier and Torsvik (2014), the northwest margin of the European Variscan Belt was accreted to Laurussia at \sim 355–335 Ma (Mississippian) following the southeast-dipping subduction of the Rheic Ocean, contemporaneously with the Paleotethys opening. After continental collision, the European Variscan Belt and Laurussia moved eastward in accordance with the westward drift of Gondwana. Consequently, during the late Carboniferous–early Permian, the boundary between the southern European Variscan Belt and the NW Gondwana became transcurrent with the development of significant strike-slip shear zones, syntectonic emplacement of granites and intracontinental basins opening. Considering paleomagnetic data and tectonic constraints, Edel et al. (2018) emphasized that the European Variscan Belt suffered a transtensional event from \sim 325 to \sim 310 Ma with the development of conjugate dextral NW–SE- and sinistral N–S-trending shear zones. Then, at \sim 310–300 Ma, a NNE–SSW compressive event, responsible for the formation of the Cantabrian orocline in the SW Variscides, occurred in the whole European Variscan Belt.

During the NNE–SSW late Carboniferous compressive event (Figure 14b-A), the MTM, Corsica and Sardinia were located to the east of the Vosges/Schwarzwald Massif, between the French Massif Central and the Bohemian Massif (Edel et al., 2018). The stretching direction in the Internal Zone of the MTM and Corso–Sardinian Block was parallel to the main tectono-metamorphic zonation of the belt, whose mean attitude in its SE part is NE–SW (Edel et al., 2018; Martínez Catalán et al., 2021). Between \sim 300 Ma and \sim 260 Ma, a major \sim 90° clockwise rotation of the MTM and the Corso–Sardinian Block (Edel et al., 2014) coincides with a N–S extension and transtensional shear zones development, which could be related to the onset of Permo-Triassic opening of the Neotethys Ocean (Edel et al., 2018). Following this clockwise rotation, the MTM and the Corso–Sardinian Block acquired a NE–SW position resulting in a ca. N–S orientation of the tectono-metamorphic zonation (Figure 14b-B). Finally, in Oligo-Miocene times (Figure 14b-C), the \sim 50° counterclockwise rotation of Corsica and Sardinia (e.g., Gattacceca et al., 2007), linked to rifting and opening of the Liguro-Provençal basin led to the current position of the Corso–Sardinian Block. These successive rotations resulted in major obliquities between the late-Variscan stretching direction, as recorded in the MTM and Corso–Sardinian Block and the NE–SW mean attitude of the SE Variscides at that time.

8. Conclusions

Fabric study and dating of the CGC and associated dykes highlight their emplacement in late Pennsylvanian to earliest Permian times (\sim 305–298 Ma) in accordance with the deformation of the surrounding migmatitic gneiss. Very strong stretching induced thinning of the continental crust associated with partial melting, granitic

intrusions and the exhumation of the lower continental crust. The MTM and the Corso–Sardinian Block reveal a quite similar tectonic evolution at the transition between late Carboniferous and early Permian. For at least 25 Ma, between ~325 and ~300 Ma, the tectonic setting is strongly marked by a strike-slip regime with heterogeneous deformation, which progressively evolves from transpression to extension with very strong stretching parallel to the orogen that produces lateral flow, thinning and exhumation of the ductile lower crust during the vanishing of the European Variscan orogeny.

Data Availability Statement

Additional methodological information and metadata for LA-ICP-MS U-Pb isotopic analyses of zircon and monazite (Supplementary Table 1), the entire zircon and monazite U-Pb data set, including both samples and reference materials (Supplementary Tables 2 and 3), raw muscovite Ar/Ar data (Supplementary Tables 4 and 5), specimen and mean AMS data, with Schmidt plots (Supplementary Table 6) and IA data, with Schmidt plots showing the individual measurements (Supplementary Table 7) are available at <https://doi.org/10.17632/jd8m75cbsm.1>. Details about the softwares utilized for processing raw data are given in the analytical methods (see Supporting Information S1). The Stereonet program by R. W. Allmendinger (available at <https://www.rickallmendinger.net/stereonet>) was used for plotting structural data and the figures were (re)drawn using Adobe Illustrator.

Acknowledgments

Bernard Charlier is thanked for the SEM analysis and Michaël Mintrone for help during sample preparation for geochronology. Jean-Bernard Edel kindly made available to us his raw AMS data on the Corsica–Sardinia Batholith in N. Sardinia and Leonardo Casini enthusiastically commented on the petrology, structure and geochronology of that part of the batholith. We also acknowledge José R. Martínez Catalán, Jiří Žák, and Leonardo Casini for their insightful and constructive reviews that significantly helped to improve the original manuscript and Taylor Schildgen for careful editorial handling.

References

- Amenzou, M. (1988). *Les granitoïdes hercyniens du massif des Maures (Var, France). Étude géologique et minéralogique. Implications génétiques*. PhD Thesis. University of Nice.
- Amenzou, M., & Pupin, J.-P. (1986). Le granite de Camarat (Maures, Var, France): Un ensemble polygénique, zone clé entre la Provence et la Corse. *Comptes Rendus des Séances de l'Académie des Sciences, Paris, Série II*, 303, 697–700.
- Amice, M. (1990). Le complexe granitique de Cabeza de Araya (Estrémadure, Espagne): Zonation, structures magmatiques et magnétiques, géométrie. In *Discussion du mode de mise en place* (Vol. 3). PhD Thesis. University of Toulouse 3.
- Archánjo, C. J., Bouchez, J.-L., Corsini, M., & Vauchez, A. (1994). The Pombal granite pluton: Magnetic fabric, emplacement and relationships with the Brasiliano strike-slip setting of NE Brazil (Paraíba State). *Journal of Structural Geology*, 16(3), 323–335. [https://doi.org/10.1016/0191-8141\(94\)90038-8](https://doi.org/10.1016/0191-8141(94)90038-8)
- Arthaud, F., & Matte, P. (1977). Late Paleozoic strike-slip faulting in southern Europe and northern Africa: Result of a right-lateral shear zone between the Appalachians and the Urals. *Geological Society of America Bulletin*, 88(9), 1305–1320. [https://doi.org/10.1130/0016-7606\(1977\)88%3C1305:1psfis%3E2.0.co;2](https://doi.org/10.1130/0016-7606(1977)88%3C1305:1psfis%3E2.0.co;2)
- Bellot, J.-P. (2005). The Palaeozoic evolution of the Maures massif (France) and its potential correlation with others areas of the Variscan belt: A review. *Journal of the Virtual Explorer*, 19(4), 1–23. <https://doi.org/10.3809/jvirtex.2005.00116>
- Bellot, J.-P., Bronner, G., & Laverne, C. (2002). Transcurrent strain partitioning along a suture zone in the Maures massif (France): Result of eastern indenter tectonics in European Variscides? In J. R. Martínez Catalán, R. D. Hatcher Jr., R. Arenas, & F. Díaz García (Eds.), *Variscan-Appalachian dynamics: The building of the late Paleozoic basement*, Geological Society of America Special Paper (Vol. 364, pp. 223–237). <https://doi.org/10.1130/0-8137-2364-7.223>
- Bellot, J.-P., Bronner, G., Marchand, J., Laverne, C., & Triboulet, C. (2002). Chevauchement et détachement dans les Maures occidentales (Var, France): Géométrie, cinématique et évolution thermobarométrique de la zone de cisaillement polyphasée de Cavalaire. *Géologie de la France*, 200(1), 21–37.
- Bellot, J.-P., Triboulet, C., Laverne, C., & Bronner, G. (2003). Evidence for two burial/exhumation stages during the evolution of the Variscan belt, as exemplified by P-T-t paths of metabasites in distinct allochthonous units of the Maures massif (SE France). *International Journal of Earth Sciences*, 92(1), 7–26. <https://doi.org/10.1007/s00531-002-0302-y>
- Benn, K. (2010). Anisotropy of magnetic susceptibility fabrics in syntectonic plutons as tectonic strain markers: The example of the Canso pluton, Meguma Terrane, Nova Scotia. *Earth and Environmental Science Transactions of the Royal Society of Edinburgh*, 100 (for 2009), 147–158. <https://doi.org/10.1017/s1755691009016028>
- Benn, K., Ham, N. M., Pignotta, G. S., & Bleeker, W. (1998). Emplacement and deformation of granites during transpression: Magnetic fabrics of the Archean Sparrow pluton, Slave Province, Canada. *Journal of Structural Geology*, 20(9–10), 1247–1259. [https://doi.org/10.1016/S0191-8141\(98\)00065-0](https://doi.org/10.1016/S0191-8141(98)00065-0)
- Benn, K., Paterson, S. R., Lund, S. P., Pignotta, G. S., & Kruse, S. (2001). Magmatic fabrics in batholiths as markers of regional strains and plate kinematics: Example of the Cretaceous Mt. Stuart batholith. *Physics and Chemistry of the Earth (Part A)*, 26(4–5), 343–354. [https://doi.org/10.1016/S1464-1895\(01\)00064-3](https://doi.org/10.1016/S1464-1895(01)00064-3)
- Bolle, O., Diot, H., Vander Auwera, J., Dembele, A., Schittekat, J., Spassov, S., et al. (2018). Pluton construction and deformation in the Sveconorwegian crust of SW Norway: Magnetic fabric and U-Pb geochronology of the Kleivan and Sjelset granitic complexes. *Precambrian Research*, 305, 247–267. <https://doi.org/10.1016/j.precamres.2017.12.012>
- Bordet, P., Guierard, S., & Nesteroff, W. (1967). *Carte géologique de la France à 1/50.000, feuille N°1047 (St-Tropez–Cap Lardier)*. BRGM.
- Borradaile, G. J., & Jackson, M. (2004). Anisotropy of magnetic susceptibility (AMS): Magnetic petrofabrics of deformed rocks. In F. Martín-Hernández, C. M. Lüneburg, C. Aubourg, & M. Jackson (Eds.), *Magnetic fabric: Methods and applications*, Geological Society, London, Special Publications (Vol. 238, pp. 299–360). <https://doi.org/10.1144/gsl.sp.2004.238.01.18>
- Bouchez, J.-L. (2000). Anisotropie de susceptibilité magnétique et fabrique des granites. *Comptes Rendus de l'Académie des Sciences, Paris, Sciences de la Terre et des Planètes*, 330, 1–14. [https://doi.org/10.1016/S1251-8050\(00\)00120-8](https://doi.org/10.1016/S1251-8050(00)00120-8)
- Bouchez, J.-L., Gleizes, G., Djouadi, T., & Rochette, P. (1990). Microstructure and magnetic susceptibility applied to emplacement kinematics of granites: The example of the Foix pluton (French Pyrenees). *Tectonophysics*, 184(2), 157–171. [https://doi.org/10.1016/0040-1951\(90\)90051-9](https://doi.org/10.1016/0040-1951(90)90051-9)

- Brown, M., & Solar, G. S. (1998). Granite ascent and emplacement during contractional deformation in convergent orogens. *Journal of Structural Geology*, 20(9–10), 1365–1393. [https://doi.org/10.1016/S0191-8141\(98\)00074-1](https://doi.org/10.1016/S0191-8141(98)00074-1)
- Buscail, F. (2000). *Contribution à la compréhension du problème géologique et géodynamique du massif des Maures: Le métamorphisme régional modélisé dans le système KFMASH – analyse paragenétique, chémiographie, thermobarométrie, géochronologie Ar/Ar*. PhD Thesis. University of Montpellier 2.
- Cagnard, F., Durrieu, N., Gapais, D., Brun, J.-B., & Ehlers, C. (2006). Crustal thickening and lateral flow during compression of hot lithospheres, with particular reference to Precambrian times. *Terra Nova*, 18(1), 72–78. <https://doi.org/10.1111/j.1365-3121.2005.00665.x>
- Cappelli, B., Carmignani, L., Castorina, F., Di Pisa, A., Oggiano, G., & Petrini, R. (1992). A Hercynian suture zone in Sardinia: Geological and geochemical evidence. *Geodinamica Acta*, 5(1–2), 101–118. <https://doi.org/10.1080/09853111.1992.11105222>
- Carmignani, L., Oggiano, G., Funedda, A., Conti, P., & Pasci, S. (2016). The geological map of Sardinia (Italy) at 1:250,000 scale. *Journal of Maps*, 12(5), 826–835. <https://doi.org/10.1080/17445647.2015.1084544>
- Carosi, R., Montomoli, C., Tiepolo, M., & Frassi, C. (2012). Geochronological constraints on post-collisional shear zones in the Variscides of Sardinia (Italy). *Terra Nova*, 24(1), 42–51. <https://doi.org/10.1111/j.1365-3121.2011.01035.x>
- Carosi, R., & Palmeri, R. (2002). Orogen-parallel tectonic transport in the Variscan belt of northeastern Sardinia (Italy): Implications for the exhumation of medium-pressure metamorphic rocks. *Geological Magazine*, 139(05), 497–511. <https://doi.org/10.1017/S0016756802006763>
- Casini, L., Cuccuru, S., Maino, M., Oggiano, G., Puccini, A., & Rossi, P. (2015). Structural map of Variscan northern Sardinia (Italy). *Journal of Maps*, 11(1), 75–84. <https://doi.org/10.1080/17445647.2014.936914>
- Casini, L., Cuccuru, S., Maino, M., Oggiano, G., & Tiepolo, M. (2012). Emplacement of the Arzachena Pluton (Corsica–Sardinia Batholith) and the geodynamics of incoming Pangaea. *Tectonophysics*, 544–545, 31–49. <https://doi.org/10.1016/j.tecto.2012.03.028>
- Casini, L., Cuccuru, S., Puccini, A., Oggiano, G., & Rossi, P. (2015). Evolution of the Corsica–Sardinia Batholith and late-orogenic shearing of the Variscides. *Tectonophysics*, 646, 65–78. <https://doi.org/10.1016/j.tecto.2015.01.017>
- Casini, L., Maino, M., Langone, A., Oggiano, G., Corvò, S., Estrada, J. R., & Liesa, M. (2023). HTLP metamorphism and fluid-fluxed melting during multistage anatexis of continental crust (N Sardinia, Italy). *Journal of Metamorphic Geology*, 41(1), 25–57. <https://doi.org/10.1111/jmg.12687>
- Cassinis, G., Perotti, C. R., & Ronchi, A. (2012). Permian continental basins in the Southern Alps (Italy) and peri-mediterranean correlations. *International Journal of Earth Sciences*, 101(1), 129–157. <https://doi.org/10.1007/s00531-011-0642-6>
- Castiñeiras, P., Villaseca, C., Barbero, L., & Romera, C. M. (2008). SHRIMP U–Pb zircon dating of anatexis in high-grade migmatite complexes of Central Spain: Implications in the Hercynian evolution of Central Iberia. *International Journal of Earth Sciences*, 97(1), 35–50. <https://doi.org/10.1007/s00531-006-0167-6>
- Clark, D. A. (1997). Magnetic petrophysics and magnetic mineralogy: Aids to geological interpretation of magnetic surveys. *Journal of Australian Geology and Geophysics*, 17, 83–103.
- Cocherie, A., Rossi, P., Fanning, C. M., & Guerrot, C. (2005). Comparative use of TIMS and SHRIMP for U–Pb zircon dating of A-type granites and mafic tholeiitic layered complexes and dykes from the Corsican Batholith (France). *Lithos*, 82(1–2), 185–219. <https://doi.org/10.1016/j.lithos.2004.12.016>
- Corsini, M., Bosse, V., Féraud, G., Demoux, A., & Crevola, G. (2010). Exhumation processes during post-collisional stage in the Variscan belt revealed by detailed $^{40}\text{Ar}/^{39}\text{Ar}$ study (Tanneron Massif, SE France). *International Journal of Earth Sciences*, 99(2), 327–341. <https://doi.org/10.1007/s00531-008-0397-x>
- Corsini, M., & Rolland, Y. (2009). Late evolution of the southern European Variscan belt: Exhumation of the lower crust in a context of oblique convergence. *Comptes Rendus de l'Académie des Sciences, Géoscience*, 341(2–3), 214–223. <https://doi.org/10.1016/j.crte.2008.12.002>
- Couziñé, S., Laurent, O., Chelle-Michou, C., Bouilhol, P., Paquette, J.-L., Gannoun, A.-M., & Moyen, J.-F. (2019). Detrital zircon U–Pb–Hf systematics of Ediacaran metasediments from the French Massif Central: Consequences for the crustal evolution of the north Gondwana margin. *Precambrian Research*, 324, 269–284. <https://doi.org/10.1016/j.precamres.2019.01.016>
- Crevola, G., Pupin, J.-P., & Toutin-Morin, N. (1991). La Provence varisque: Structure et évolution géologique anté-triasique. *Sciences Géologiques, Bulletin*, 44(3), 287–310. <https://doi.org/10.3406/sgeol.1991.1869>
- Demoux, A., Schärer, U., & Corsini, M. (2008). Variscan evolution of the Tanneron massif, SE France, examined through U–Pb monazite ages. *Journal of the Geological Society, London*, 165, 467–478. <https://doi.org/10.1144/0016-76492007-045>
- D'Lemos, R. S., Brown, M., & Strachan, R. A. (1992). Granite magma generation, ascent and emplacement within a transpressional orogen. *Journal of the Geological Society, London*, 149, 487–490. <https://doi.org/10.1144/gsjgs.149.4.0487>
- Domeier, M., & Torsvik, T. H. (2014). Plate tectonics in the late Paleozoic. *Geoscience Frontiers*, 5(3), 303–350. <https://doi.org/10.1016/j.gsf.2014.01.002>
- Duchesne, J.-C., Liégeois, J.-P., Bolle, O., Vander Auwera, J., Bruguier, O., Matukov, D. I., & Sergeev, S. A. (2013). The fast evolution of a crustal hot zone at the end of a transpressional regime: The Saint-Tropez peninsula granites and related dykes (Maures Massif, SE France). *Lithos*, 162–163, 195–220. <https://doi.org/10.1016/j.lithos.2012.12.019>
- Duclaux, G., Rey, P., Guillot, S., & Ménot, R.-P. (2007). Orogen-parallel flow during continental convergence: Numerical experiments and Archean field examples. *Geology*, 35(8), 715–718. <https://doi.org/10.1130/G23540a.1>
- Dunlop, D. J. (2014). High-temperature susceptibility of magnetite: A new pseudo-single-domain effect. *Geophysical Journal International*, 199(2), 707–716. <https://doi.org/10.1093/gji/ggu247>
- Dunlop, D. J., & Özdemir, Ö. (2015). Magnetizations in rocks and minerals. In M. Kono (Ed.), *Treatise of Geophysics, Vol. 5 (Geomagnetism)* (2d ed., pp. 256–308). Elsevier. <https://doi.org/10.1016/B978-0-444-53802-4.00102-0>
- Dunlop, D. J., Özdemir, Ö., & Rancourt, D. G. (2006). Magnetism of biotite crystals. *Earth and Planetary Science Letters*, 243(3–4), 805–819. <https://doi.org/10.1016/j.epsl.2006.01.048>
- Durand, M. (2008). Permian to Triassic continental successions in southern Provence (France): An overview. *Bollettino della Società Geologica Italiana*, 127, 697–716.
- Edel, J.-B., Casini, L., Oggiano, G., Rossi, P., & Schulmann, K. (2014). Early Permian 90° clockwise rotation of the Maures–Estérel–Corsica–Sardinia block confirmed by new palaeomagnetic data and followed by a Triassic 60° clockwise rotation. In K. Schulmann, J. R. Martínez Catalán, J.-M. Lardeaux, V. Janoušek, & G. Oggiano (Eds.), *The Variscan orogeny: extent, timescale and the formation of the European crust*, Geological Society, London, Special Publications (Vol. 405, pp. 333–361). <https://doi.org/10.1144/sp405.10>
- Edel, J.-B., Schulmann, K., Lexa, O., & Lardeaux, J.-M. (2018). Late Palaeozoic palaeomagnetic and tectonic constraints for amalgamation of Pangea supercontinent in the European Variscan belt. *Earth-Science Reviews*, 177, 589–612. <https://doi.org/10.1016/j.earscirev.2017.12.007>
- Faure, M., Lardeaux, J.-M., & Ledru, P. (2009). A review of the pre-Permian geology of the Variscan French Massif Central. *Comptes Rendus Geoscience*, 341(2–3), 202–213. <https://doi.org/10.1016/j.crte.2008.12.001>

- Ferré, E., Gleizes, G., Djouadi, M. T., & Bouchez, J.-L. (1997). Drainage and emplacement of magmas along an inclined transcurrent shear zone: Petrophysical evidence from a granite-charnockite pluton (Rahama, Nigeria). In J.-L. Bouchez, D. H. W. Hutton, & W. E. Stephens (Eds.), *Granite: From segregation of melt to emplacement fabrics* (pp. 253–273). Kluwer. https://doi.org/10.1007/978-94-017-1717-5_16
- Franke, W. (1989). Tectonostratigraphic units in the Variscan belt of central Europe. *Geological Society of America, Special paper*, 230, 67–90. <https://doi.org/10.1130/spe230-p67>
- Franke, W., Cocks, L. R. M., & Torsvik, T. H. (2017). The Palaeozoic Variscan oceans revisited. *Gondwana Research*, 48, 257–284. <https://doi.org/10.1016/j.gr.2017.03.005>
- Frassi, C., Carosi, R., Montomoli, C., & Law, R. D. (2009). Kinematics and vorticity of flow associated with post-collisional oblique transpression in the Variscan Inner Zone of northern Sardinia (Italy). *Journal of Structural Geology*, 31(12), 1458–1471. <https://doi.org/10.1016/j.jsg.2009.10.001>
- Gattacceca, J., Deino, A., Rizzo, R., Jones, D. S., Henry, B., Beaudoin, B., & Vadeboin, F. (2007). Miocene rotation of Sardinia: New paleomagnetic and geochronological constraints and geodynamic implications. *Earth and Planetary Science Letters*, 258(3–4), 359–377. <https://doi.org/10.1016/j.epsl.2007.02.003>
- Gattacceca, J., Orsini, J.-B., Bellot, J.-P., Henry, B., Rochette, P., Rossi, P., & Cherchi, G. (2004). Magnetic fabric of granitoids from southern Corsica and northern Sardinia and implications for late Hercynian tectonic setting. *Journal of the Geological Society, London*, 161, 277–289. <https://doi.org/10.1144/0016-764903-115>
- Gébelin, A., Martelet, G., Chen, Y., Brunel, M., & Faure, M. (2006). Structure of late Variscan Millevaches leucogranite massif in the French Massif Central: AMS and gravity modelling results. *Journal of Structural Geology*, 28(1), 148–169. <https://doi.org/10.1016/j.jsg.2005.05.021>
- Gerbault, M., Schneider, J., Reverso-Peila, A., & Corsini, M. (2018). Crustal exhumation during ongoing compression in the Variscan Maures-Tanneron Massif, France—Geological and thermo-mechanical aspects. *Tectonophysics*, 746, 439–458. <https://doi.org/10.1016/j.tecto.2016.12.019>
- Giacomini, F., Dallai, L., Carminati, E., Tiepolo, M., & Ghezzi, C. (2008). Exhumation of a Variscan orogenic complex: Insights into the composite granulitic-amphibolitic metamorphic basement of south-east Corsica (France). *Journal of Metamorphic Geology*, 26(4), 403–436. <https://doi.org/10.1111/j.1525-1314.2008.00768.x>
- Gleizes, G., Leblanc, D., Santana, V., Olivier, P., & Bouchez, J.-L. (1998). Sigmoidal structures featuring dextral shear during emplacement of the Hercynian granite complex of Causerets–Panticosa (Pyrenees). *Journal of Structural Geology*, 20(9–10), 1229–1245. [https://doi.org/10.1016/S0191-8141\(98\)00060-1](https://doi.org/10.1016/S0191-8141(98)00060-1)
- Gueguen, E. (1995). *Segmentation des marges et processus d'amincissement crustal: l'exemple du bassin liguro-provençal*. PhD Thesis. University of Brest.
- Guillot, S., & Ménot, R.-P. (2009). Paleozoic evolution of the external Crystalline Massifs of the Western Alps. *Comptes Rendus Geoscience*, 341(2–3), 253–265. <https://doi.org/10.1016/j.crte.2008.11.010>
- Haggerty, S. E. (1991). Oxide textures – A mini-atlas. In D. H. Lindsley (Ed.), *Oxide minerals: Petrologic and magnetic significance*, *Reviews in Mineralogy* (Vol. 25, pp. 129–219). <https://doi.org/10.1515/9781501508684-008>
- Harlov, D. E., Wirth, R., & Hetherington, C. J. (2011). Fluid-mediated partial alteration in monazite: The role of coupled dissolution-reprecipitation in element redistribution and mass transfer. *Contributions to Mineralogy and Petrology*, 162(2), 329–348. <https://doi.org/10.1007/s00410-010-0599-7>
- Henry, B., Jordanova, D., Jordanova, N., Souque, C., & Robion, P. (2003). Anisotropy of magnetic susceptibility of heated rocks. *Tectonophysics*, 366(3–4), 241–258. [https://doi.org/10.1016/S0040-1951\(03\)00099-4](https://doi.org/10.1016/S0040-1951(03)00099-4)
- Hrouda, F. (1994). A technique for the measurement of thermal changes of magnetic susceptibility of weakly magnetic rocks by the CS-2 apparatus and KLY-2 Kappabridge. *Geophysical Journal International*, 118(3), 604–612. <https://doi.org/10.1111/j.1365-246X.1994.tb03987.x>
- Hrouda, F., Jelínek, V., & Zapletal, K. (1997). Refined technique for susceptibility resolution into ferromagnetic and paramagnetic components based on susceptibility temperature-variation measurement. *Geophysical Journal International*, 129(3), 715–719. <https://doi.org/10.1111/j.1365-246X.1997.tb04506.x>
- Hutton, D. H. W. (1988). Granite emplacement mechanisms and tectonic controls: Inferences from deformation studies. *Transactions of the Royal Society of Edinburgh, Earth Sciences*, 79(2–3), 245–255. <https://doi.org/10.1017/S0263593300014255>
- Innocent, C., Michard, A., Guerrot, C., & Hamelin, B. (2003). Datation U-Pb sur zircons à 548 Ma de leptynites des Maures centrales. Signification géodynamique des complexes leptyno-amphibolitiques de l'Europe varisque. *Bulletin de la Société Géologique de France*, 174(6), 585–594. <https://doi.org/10.2113/174.6.585>
- Jelínek, V. (1981). Characterization of magnetic fabric of rocks. *Tectonophysics*, 79(3–4), T63–T67. [https://doi.org/10.1016/0040-1951\(81\)90110-4](https://doi.org/10.1016/0040-1951(81)90110-4)
- Jolivet, L., Romagny, A., Gorini, C., Maillard, A., Thion, I., Couëffé, R., et al. (2020). Fast dismantling of a mountain belt by mantle flow: Late-orogenic evolution of Pyrenees and Liguro-Provençal rifting. *Tectonophysics*, 776, 228312. <https://doi.org/10.1016/j.tecto.2019.228312>
- Langone, A., Zanetti, A., Daczko, N. R., Piazzolo, S., Tiepolo, M., & Mazzucchelli, M. (2018). Zircon U-Pb dating of a lower crustal shear zone: A case study from the northern sector of the Ivrea-Verbano zone (Val Cannobina, Italy). *Tectonics*, 37(1), 322–342. <https://doi.org/10.1029/2017tc004638>
- Laurent, O., Couzinié, S., Zeh, A., Vanderhaeghe, O., Moyen, J.-F., Villaros, A., et al. (2017). Protracted, coeval crust and mantle melting during Variscan late-orogenic evolution: U-Pb dating in the eastern French Massif Central. *International Journal of Earth Sciences*, 106(2), 421–451. <https://doi.org/10.1007/s00531-016-1434-9>
- Li, X.-H., Faure, M., & Lin, W. (2014). From crustal anatexis to mantle melting in the Variscan orogen of Corsica (France): SIMS U-Pb zircon age constraints. *Tectonophysics*, 634, 19–30. <https://doi.org/10.1016/j.tecto.2014.07.021>
- Martínez Catalán, J. R., Schulmann, K., & Ghienne, J.-F. (2021). The Mid-Variscan Allochthon: Keys from correlation, partial retrodeformation and plate-tectonic reconstruction to unlock the geometry of a non-cylindrical belt. *Earth-Science Reviews*, 220, 103700. <https://doi.org/10.1016/j.earscirev.2021.103700>
- Matte, P. (2001). The Variscan collage and orogeny (480–290 Ma) and the tectonic definition of the Armorica microplate: A review. *Terra Nova*, 13(2), 122–128. <https://doi.org/10.1046/j.1365-3121.2001.00327.x>
- Morillon, A.-C., Féraud, G., Sosson, M., Ruffet, G., Crevola, G., & Lerouge, G. (2000). Diachronous cooling on both sides of a major strike slip fault in the Variscan Maures Massif (south-east France), as deduced from a detailed ⁴⁰Ar/³⁹Ar study. *Tectonophysics*, 321(1), 103–126. [https://doi.org/10.1016/S0040-1951\(00\)00076-7](https://doi.org/10.1016/S0040-1951(00)00076-7)
- Moussavou, M. (1998). *Contribution à l'histoire thermo-tectonique varisque du massif des Maures, par la typologie du zircon et la géochronologie U/Pb sur minéraux accessoires (Var, France)*. PhD Thesis. University of Montpellier 2.
- Oggiano, G., Aversano, A., Cherchi, G. P., Di Pisa, A., Orrù, P., Ulzega, A., et al. (2015). *Note illustrative della Carta Geologica d'Italia alla scala 1:50.000, Foglio 412 (La Maddalena)*. ISPRA, Servizio Geologico d'Italia.

- Oggiano, G., Cherchi, G. P., Pisanu, G., Murtas, A., Patta, E. D., Prochilo, F., et al. (2014). *Note illustrative della Carta Geologica d'Italia alla scala 1:50.000, Foglio 443 (Tempio Pausania)*. ISPRA, Servizio Geologico d'Italia.
- Oliot, E., Melleton, J., Schneider, J., Corsini, M., Gardien, V., & Rolland, Y. (2015). Variscan crustal thickening in the Maures-Tanneron massif (south Variscan belt, France): New in situ monazite U-Th-Pb chemical dating of high-grade rocks. *Bulletin de la Société Géologique de France*, 186(2–3), 145–169. <https://doi.org/10.2113/gssgfbull.186.2-3.145>
- Onézime, J., Faure, M., & Crevola, G. (1999). Étude pétro-structurale du complexe granitique Rouet – Plan-de-la-Tour (massifs des Maures et du Tanneron occidental, Var). *Comptes Rendus de l'Académie des Sciences, Paris, Série IIa*, 328(11), 773–779. [https://doi.org/10.1016/s1251-8050\(99\)80170-0](https://doi.org/10.1016/s1251-8050(99)80170-0)
- Orsini, J.-B., Ferrandini, J., Ferrandini, M., Loÿe, M.-D., Guennoc, P., Pluquet, F., et al. (2011). *Carte géologique de la France à 1/50.000, feuille N°1127 (Sotta-Bonifacio-Santa Teresa di Gallura)*. BRGM.
- Padovano, M., Dörr, W., Elter, F. M., & Gerdes, A. (2014). The East Variscan shear zone: Geochronological constraints from the Capo Ferro area (NE Sardinia, Italy). *Lithos*, 196–197, 27–41. <https://doi.org/10.1016/j.lithos.2014.01.015>
- Paquette, J.-L., Ménot, R.-P., Pin, C., & Orsini, J.-B. (2003). Episodic and short-lived granitic pulses in a post-collisional setting: Evidence from precise U-Pb zircon dating through a crustal cross-section in Corsica. *Chemical Geology*, 198(1–2), 1–20. [https://doi.org/10.1016/s0009-2541\(02\)00401-1](https://doi.org/10.1016/s0009-2541(02)00401-1)
- Passchier, C. W., & Trouw, R. A. J. (2005). *Microtectonics* (2d ed.). Springer-Verlag. <https://doi.org/10.1007/3-540-29359-0>
- Pelletier, A., Gapais, D., Ménot, R.-P., & Peucat, J.-J. (2002). Tectonique transpressive en terre Adélie au Paléoproterozoïque (Est Antarctique). *C. R. Geoscience*, 334(7), 505–511. [https://doi.org/10.1016/s1631-0713\(02\)01777-7](https://doi.org/10.1016/s1631-0713(02)01777-7)
- Pereira, M. F., Silva, J. B., Drost, K., Chichorro, M., & Apraiz, A. (2010). Relative timing of transcurrent displacements in northern Gondwana: U-Pb laser ablation ICP-MS zircon and monazite geochronology of gneisses and sheared granites from the Western Iberian Massif (Portugal). *Gondwana Research*, 17(2–3), 461–481. <https://doi.org/10.1016/j.gr.2009.08.006>
- Petrovský, E., & Kapička, A. (2006). On determination of the Curie point from thermomagnetic curves. *Journal of Geophysical Research*, 111(B12), B12S27. <https://doi.org/10.1029/2006jb004507>
- Porquet, M., Pueyo, E. L., Román-Berdiel, T., Olivier, P., Longares, L. A., Cuevas, J., et al. (2017). Anisotropy of magnetic susceptibility of the Pyrenean granites. *Journal of Maps*, 13(2), 438–448. <https://doi.org/10.1080/17445647.2017.1302364>
- Potter, D. K., & Stephenson, A. (1988). Single-domain particles in rocks and magnetic fabric analysis. *Geophysical Research Letters*, 15(10), 1097–1100. <https://doi.org/10.1029/g1015i010p01097>
- Renna, M. R., Tribuzio, R., & Tiepolo, M. (2007). Origin and timing of the post-Variscan gabbro-granite complex of Porto (Western Corsica). *Contributions to Mineralogy and Petrology*, 154(5), 493–517. <https://doi.org/10.1007/s00410-007-0205-9>
- Richter, C., & van der Pluijm, B. A. (1994). Separation of paramagnetic and ferrimagnetic susceptibilities using low temperature magnetic susceptibilities and comparison with high field methods. *Physics of the Earth and Planetary Interiors*, 82(2), 113–123. [https://doi.org/10.1016/0031-9201\(94\)90084-1](https://doi.org/10.1016/0031-9201(94)90084-1)
- Rochette, P. (1987). Magnetic susceptibility of the rock matrix related to magnetic fabric studies. *Journal of Structural Geology*, 9(8), 1015–1020. [https://doi.org/10.1016/0191-8141\(87\)90009-5](https://doi.org/10.1016/0191-8141(87)90009-5)
- Rochette, P., Jackson, M., & Aubourg, C. (1992). Rock magnetism and the interpretation of anisotropy of magnetic susceptibility. *Reviews of Geophysics*, 30(3), 209–226. <https://doi.org/10.1029/92rg00733>
- Rolin, P., Marquer, D., Colchen, M., Cartannaz, C., Cocherie, A., Thiery, V., et al. (2009). Famenco-Carboniferous (370–320 Ma) strike slip tectonics monitored by syn-kinematic plutons in the French Variscan belt (Massif Armoricain and French Massif Central). *Bulletin de la Société Géologique de France*, 180(3), 231–246. <https://doi.org/10.2113/gssgfbull.180.3.231>
- Rolland, Y., Corsini, M., & Demoux, A. (2009). Metamorphic and structural evolution of the Maures-Tanneron massif (SE Variscan chain): Evidence of doming along a transpressional margin. *Bulletin de la Société Géologique de France*, 180(3), 217–230. <https://doi.org/10.2113/gssgfbull.180.3.217>
- Rossi, P., & Cocherie, A. (1991). Genesis of a Variscan batholith: Field, petrological and mineralogical evidence from the Corsica-Sardinia batholith. *Tectonophysics*, 195(2–4), 319–346. [https://doi.org/10.1016/0040-1951\(91\)90219-i](https://doi.org/10.1016/0040-1951(91)90219-i)
- Rossi, P., Cocherie, A., & Fanning, C. M. (2015). Evidence in Variscan Corsica of a brief and voluminous Late Carboniferous to Early Permian volcanic-plutonic event contemporaneous with a high-temperature/low-pressure metamorphic peak in the lower crust. *Bulletin de la Société Géologique de France*, 186(2–3), 171–192. <https://doi.org/10.2113/gssgfbull.186.2-3.171>
- Roubault, M., Bordet, P., Leutwein, F., Sonet, J., & Zimmermann, J.-L. (1970). Ages absolus des formations cristallophylliennes des Massifs des Maures et du Tanneron. *Comptes Rendus de l'Académie des Sciences, Paris, Série D*, 271, 1067–1070.
- Rouire, J., Bodelle, J., Autran, A., Bordet, B., Beaudoin, B., Gigot, P., et al. (1979). *Carte géologique de la France à 1/250.000, feuille N°40 (Nice)*. BRGM.
- Rouire, J., L'Homer, A., Blanc, J.-J., & Gabert, J. (1979). *Carte géologique de la France à 1/250.000, feuille N°39 (Marseille)*. BRGM.
- Schnapperelle, S., Mezger, J. E., Stipp, M., Hofmann, M., Gärtner, A., & Linnemann, U. (2020). Polyphase magmatic pulses along the northern Gondwana margin: U-Pb zircon geochronology from gneiss domes of the Pyrenees. *Gondwana Research*, 81, 291–311. <https://doi.org/10.1016/j.gr.2019.11.013>
- Schneider, J., Corsini, M., Reverso-Peila, A., & Lardeaux, J.-M. (2014). Thermal and mechanical evolution of an orogenic wedge during Variscan collision: An example in the Maures-Tanneron Massif (SE France). In K. Schulmann, J. R. Martínez Catalán, J.-M. Lardeaux, V. Janoušek, & G. Oggiano (Eds.), *The Variscan orogeny: extent, timescale and the formation of the European crust*, Geological Society, London, *Special Publications* (Vol. 405, pp. 313–331). <https://doi.org/10.1144/sp405.4>
- Simonetti, M., Carosi, R., Montomoli, C., Corsini, M., Petrocchia, A., Cottle, J. M., & Iaccarino, S. (2020). Timing and kinematics of flow in a transpressive dextral shear zone, Maures Massif (Southern France). *International Journal of Earth Sciences*, 109(7), 2261–2285. <https://doi.org/10.1007/s00531-020-01898-6>
- Stacey, J. S., & Kramers, J. D. (1975). Approximation of terrestrial lead isotope evolution by a two-stage model. *Earth and Planetary Science Letters*, 26(2), 207–221. [https://doi.org/10.1016/0012-821x\(75\)90088-6](https://doi.org/10.1016/0012-821x(75)90088-6)
- Stephan, T., Kroner, U., & Romer, R. L. (2019). The pre-orogenic detrital zircon record of the Peri-Gondwanan crust. *Geological Magazine*, 156(2), 281–307. <https://doi.org/10.1017/s0016756818000031>
- Stipp, M., Stünitz, H., Heilbronner, R., & Schmid, S. M. (2002). The eastern Tonale fault zone: A 'natural laboratory' for crystal plastic deformation of quartz over a temperature range from 250 to 700°C. *Journal of Structural Geology*, 24(12), 1861–1884. [https://doi.org/10.1016/s0191-8141\(02\)00035-4](https://doi.org/10.1016/s0191-8141(02)00035-4)
- Tabaud, A. S., Lardeaux, J.-M., & Corsini, M. (2022). A vestige of an Ediacaran magmatic arc in southeast France and its significance for the northern Gondwana margin. *International Journal of Earth Sciences*, 112(3), 925–950. <https://doi.org/10.1007/s00531-022-02277-z>

- Toutin-Morin, N., & Bonijoly, D. (1992). Structuration des bassins de Provence orientale à la fin de l'ère primaire. *Cuadernos de Geología Iberica*, 16, 59–74.
- Toutin-Morin, N., Bonijoly, D., Brocard, C., Broutin, J., Crevola, G., Dardeau, G., et al. (1994). *Carte géologique de la France à 1/50.000, feuille N°1024 (Fréjus–Cannes)*. BRGM.
- Toutin-Morin, N., Bonijoly, D., Brocard, C., Dardeau, G., & Dubar, M. (1993). Enregistrement sédimentaire de l'évolution post-hercynienne en bordure des Maures et du Tanneron du Carbonifère supérieur à l'Actuel. *Géologie de la France*, 1993(2), 3–22.
- Traversa, G., Ronca, S., Del Moro, A., Pasquali, C., Buraglini, N., & Barabino, G. (2003). Late to post-Hercynian dyke activity in the Sardinia-Corsica domain: A transition from orogenic calc-alkaline to anorogenic alkaline magmatism. *Bollettino della Società geologica italiana, Volume speciale*, 2, 131–152.
- Trindade, R. I. F., Mints Mi Nguema, T., & Bouchez, J.-L. (2001). Thermally enhanced mimetic fabric of magnetite in a biotite granite. *Geophysical Research Letters*, 28(14), 2687–2690. <https://doi.org/10.1029/2001gl013218>
- Vanderhaeghe, O., Laurent, O., Gardien, V., Moyen, J.-F., Gébelin, A., Chelle-Michou, C., et al. (2020). Flow of partially molten crust controlling construction, growth and collapse of the Variscan orogenic belt: The geologic record of the French Massif Central. *Bulletin de la Société Géologique de France*, 191, 25. <https://doi.org/10.1051/bsgf/2020013>
- Vauchez, A., & Bufalo, M. (1985). La limite Maures occidentales-Maures orientales (Var, France): Un décrochement ductile senestre majeur entre deux provinces structurales très contrastées. *Comptes Rendus des Séances de l'Académie des Sciences, Paris, Série II*, 301, 1059–1062.
- Wawrzynitz, N., Krohe, A., Rhede, D., & Romer, R. L. (2012). Dating rock deformation with monazite: The impact of dissolution precipitation creep. *Lithos*, 134–135, 52–74. <https://doi.org/10.1016/j.lithos.2011.11.025>
- Wayne, D. M., & Sinha, A. K. (1988). Physical and chemical response of zircons to deformation. *Contributions to Mineralogy and Petrology*, 98(1), 109–121. <https://doi.org/10.1007/bf00371915>
- Westphal, M., Orsini, J., & Vellutini, P. (1976). Le microcontinent corso-sarde, sa position initiale: Données paléomagnétiques et raccords géologiques. *Tectonophysics*, 30(1–2), 141–157. [https://doi.org/10.1016/0040-1951\(76\)90142-6](https://doi.org/10.1016/0040-1951(76)90142-6)
- Zheng, J. S., Mermet, J.-F., Toutin-Morin, N., Hanes, J., Gondolo, A., Morin, R., & Féraud, G. (1992). Datation ^{40}Ar - ^{39}Ar du magmatisme et de filons minéralisés permien en Provence orientale (France). *Geodinamica Acta*, 5(3), 203–215. <https://doi.org/10.1080/09853111.1992.11105228>
- Ziegler, P. A., & Stampfli, G. M. (2001). Late Palaeozoic-early Mesozoic plate boundary reorganization: Collapse of the Variscan orogen and opening of Neotethys. In G. Cassinis (Ed.), *Permian continental deposits of Europe and other areas, Regional reports and correlations, 'Natura Bresciana', Annali del Museo Civico di Scienze Naturali di Brescia, Monografia* (Vol. 25, pp. 17–34).

References From the Supporting Information

- Black, L. P., Kamo, S. L., Allen, C. M., Aleinikoff, J. N., Davis, D. W., Korsch, R. J., & Foudoulis, C. (2003). TEMORA 1: A new zircon standard for Phanerozoic U-Pb geochronology. *Chemical Geology*, 200(1–2), 155–170. [https://doi.org/10.1016/s0009-2541\(03\)00165-7](https://doi.org/10.1016/s0009-2541(03)00165-7)
- Chadima, M., & Hrouda, F. (2012). *Cureval 8.0.2, thermomagnetic curve analyzer for Windows*. Agico Inc. Retrieved from <https://www.agico.com/text/software/cureval/cureval.php>
- Gasquet, D., Bertrand, J.-M., Paquette, J.-L., Lehmann, J., Ratzov, G., De Ascensão Guedes, R., et al. (2010). Miocene to Messinian deformation and hydrothermal activity in a pre-Alpine basement massif of the French Western Alps: New U-Th-Pb and argon ages from the Lauzière massif. *Bulletin de la Société Géologique de France*, 181(3), 227–241. <https://doi.org/10.2113/gssgfbull.181.3.227>
- Gonçalves, G. E., Lana, C., Scholz, R., Buick, I. S., Gerdes, A., Kamo, S. L., et al. (2016). An assessment of monazite from the Itambé pegmatite district for use as U-Pb isotope reference material for microanalysis and implications for the origin of the 'Moacyr' monazite. *Chemical Geology*, 424, 30–50. <https://doi.org/10.1016/j.chemgeo.2015.12.019>
- Guillong, M., Wotzlaw, J.-F., Looser, N., & Laurent, O. (2020). Evaluating the reliability of U-Pb laser ablation inductively coupled plasma mass spectrometry (LA-ICP-MS) carbonate geochronology: Matrix issues and a potential calcite validation reference material. *Geochronology*, 2(1), 155–167. <https://doi.org/10.5194/gchron-2-155-2020>
- Hellstrom, J. C., Paton, C., Woodhead, J. D., & Hergt, J. M. (2008). Lolite: Software for spatially resolved LA-(quad and MC) ICP-MS analysis. In P. Sylvester (Ed.), *Laser ablation ICP-MS in the Earth sciences: Current practices and outstanding issues, Mineralogical Association of Canada Short Course series* (Vol. 40, pp. 343–348).
- Hext, G. R. (1963). The estimation of second-order tensors, with related tests and designs. *Biometrika*, 50(3/4), 353–373. <https://doi.org/10.2307/2333905>
- Horstwood, M. S. A., Košler, J., Gehrels, G., Jackson, S. E., McLean, N. M., Paton, C., et al. (2016). Community-derived standards for LA-ICP-MS U-(Th)-Pb geochronology – Uncertainty Propagation, Age interpretation and data Reporting. *Geostandards and Geoanalytical Research*, 40(3), 311–332. <https://doi.org/10.1111/j.1751-908x.2016.00379.x>
- Kennedy, A. K., Wotzlaw, J.-F., Schaltegger, U., Crowley, J. L., & Schmitz, M. (2014). Eocene zircon reference material for microanalysis of U-Th-Pb isotopes and trace elements. *The Canadian Mineralogist*, 52(3), 409–421. <https://doi.org/10.3749/canmin.52.3.409>
- Koppers, A. A. P. (2002). ArArCALC software for $^{40}\text{Ar}/^{39}\text{Ar}$ age calculations. *Computers & Geosciences*, 28(5), 605–619. [https://doi.org/10.1016/s0098-3004\(01\)00095-4](https://doi.org/10.1016/s0098-3004(01)00095-4)
- Launeau, P., & Robin, P.-Y. F. (1996). Fabric analysis using the intercept method. *Tectonophysics*, 267(1–4), 91–119. [https://doi.org/10.1016/s0040-1951\(96\)00091-1](https://doi.org/10.1016/s0040-1951(96)00091-1)
- Launeau, P., & Robin, P.-Y. F. (2005). Determination of fabric and strain ellipsoids from measured sectional ellipses – Implementation and applications. *Journal of Structural Geology*, 27(12), 2223–2233. <https://doi.org/10.1016/j.jsg.2005.08.003>
- Lee, J.-Y., Marti, K., Severinghaus, J. P., Kawamura, K., Yoo, H.-S., Lee, J. B., & Kim, J. S. (2006). A redetermination of the isotopic abundances of atmospheric Ar. *Geochimica et Cosmochimica Acta*, 70(17), 4507–4512. <https://doi.org/10.1016/j.gca.2006.06.1563>
- Paquette, J.-L., & Tiepolo, M. (2007). High resolution (5 μm) U-Th-Pb isotope dating of monazite with excimer laser ablation (ELA)-ICPMS. *Chemical Geology*, 240(3–4), 222–237. <https://doi.org/10.1016/j.chemgeo.2007.02.014>
- Paton, C., Woodhead, J. D., Hellstrom, J. C., Hergt, J. M., Greig, A., & Maas, R. (2010). Improved laser ablation U-Pb zircon geochronology through robust downhole fractionation correction. *Geochemistry, Geophysics, Geosystems*, 11(3), 1–36. <https://doi.org/10.1029/2009gc002618>
- Petrus, J. A., & Kamber, B. S. (2012). VizualAge: A novel approach to laser ablation ICP-MS U-Pb geochronology data reduction. *Geostandards and Geoanalytical Research*, 36(3), 24–270. <https://doi.org/10.1111/j.1751-908x.2012.00158.x>
- Sláma, J., Košler, J., Condon, D. J., Crowley, J. L., Gerdes, A., Hanchar, J. M., et al. (2008). Plešovice zircon – A new natural reference material for U-Pb and Hf isotopic microanalysis. *Chemical Geology*, 249(1–2), 1–35. <https://doi.org/10.1016/j.chemgeo.2007.11.005>

- Steiger, R. H., & Jäger, E. (1977). Subcommittee on geochronology: Convention on the use of decay constants in geo- and cosmochemistry. *Earth and Planetary Science Letters*, 36(3), 359–362. [https://doi.org/10.1016/0012-821x\(77\)90060-7](https://doi.org/10.1016/0012-821x(77)90060-7)
- Turner, G., Huneke, J. C., Podosek, F. A., & Wasserburg, G. J. (1971). ^{40}Ar - ^{39}Ar ages and cosmic ray exposure ages of Apollo 14 samples. *Earth and Planetary Science Letters*, 12(1), 19–35. [https://doi.org/10.1016/0012-821x\(71\)90051-3](https://doi.org/10.1016/0012-821x(71)90051-3)
- Vermeesch, P. (2018). IsoplotR: A free and open toolbox for geochronology. *Geoscience Frontiers*, 9(5), 1479–1493. <https://doi.org/10.1016/j.gsf.2018.04.001>
- Wiedenbeck, M., Allé, P., Corfu, F., Griffin, W., Meier, M., Oberli, F., et al. (1995). Three natural zircon standards for U-Th-Pb, Lu-Hf, trace element and REE analyses. *Geostandards Newsletter*, 19, 1–23. <https://doi.org/10.1111/j.1751-908x.1995.tb00147.x>